iScience

CellPress
OPEN ACCESS

Article

Hypoxia-activated probe for NIR fluorescence and photoacoustic dual-mode tumor imaging

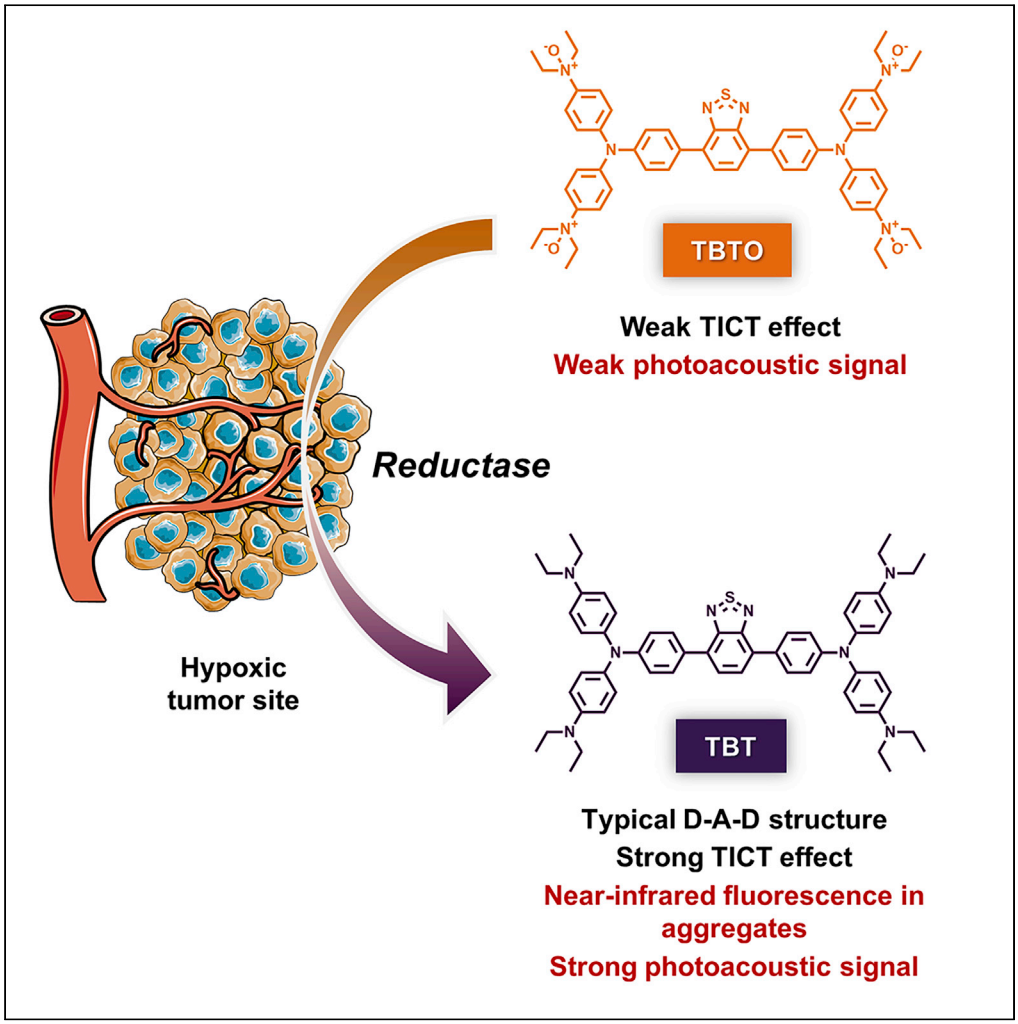

Meng Li, Huan Li, Qian Wu, ..., Ying Li, Dong Wang, Ben Zhong Tang

liyingway@szu.edu.cn (Y.L.)
wangd@szu.edu.cn (D.W.)
tangbenz@ust.hk (B.Z.T.)

HIGHLIGHTS

Hypoxia-activable probe TBTO could be converted to TBT in reductive environment

TBT exhibited red-shifted fluorescence and promoted photoacoustic signal

TBTO was well-performed in fluorescence and photoacoustic dual-mode tumor imaging

Li et al., iScience *24*, 102261
March 19, 2021
https://doi.org/10.1016/j.isci.2021.102261

iScience

CellPress
OPEN ACCESS

Article

Hypoxia-activated probe for NIR fluorescence and photoacoustic dual-mode tumor imaging

Meng Li,[1,2,5] Huan Li,[4,5] Qian Wu,[1,2] Niu Niu,[1,2] Jiachang Huang,[1,2] Lingmin Zhang,[4] Ying Li,[1,*] Dong Wang,[1,*] and Ben Zhong Tang[3,6,*]

SUMMARY

Construction of tumor microenvironment responsive probe with more than one imaging modality, in particular toward hypoxia of solid tumors, is an appealing yet significantly challenging task. In this work, we designed a hypoxia-activated probe TBTO (Triphenylamine-Benzothiadiazole-Triphenylamine derivative featuring four diethylamino N-Oxide groups) for *in vivo* imaging. TBTO could undergo bioreduction in a hypoxic microenvironment to yield compound TBT sharing both near-infrared (NIR) aggregation-induced emission and strong twisted intramolecular charge transfer features, which endows the probe with excellent performance in NIR fluorescence and photoacoustic dual-mode tumor imaging. This study offers useful insights into designing a new generation agent for clinical cancer diagnosis.

INTRODUCTION

It is generally accepted that the rapid proliferation of tumor cells and abnormal vasculature in solid tumors could result in an inadequate supply of oxygen and thus lead to a hypoxic microenvironment, which is strongly associated with tumor propagation, malignant progression, and treatment resistance (Brown and Wilson, 2004; Harris, 2002; Rankin et al., 2016). Rapid and specific hypoxia detection *in vivo* is therefore of great importance in both scientific and clinical perspectives. On the other hand, hypoxia, as a symptom of a majority of solid tumors, can also serve as an internal stimulus to activate probes for specific tumor imaging with high contrast (Liu et al., 2017; Rey et al., 2017; Zhang et al., 2009).

Photoacoustic (PA) imaging is a rapidly emerging technique that provides three-dimensional information on the distribution of endogenous biomolecules using label-free PA imaging techniques (Hai et al., 2019; Wang et al., 2013; Wong et al., 2017; Yao et al., 2015) or exogenous PA probes in real-time noninvasively (Knox and Chan, 2018; Ou et al., 2019; Weber et al., 2016). Upon irradiation with a short-pulsed laser, the PA agents absorb the energy and partially convert it to heat, resulting in a local temperature increase and thermoelastic expansion. The pressure waves propagating through the surrounding tissue can be detected via ultrasound transducers. The ultrasound signal is much less scattered in biological tissue than the optical signal, which enables high-resolution PA imaging even at centimeter depths (Liu et al., 2016; Mallidi et al., 2011). Despite these merits, activatable PA agents, which show PA signal only in the presence of specific stimuli, have rarely been reported for *in vivo* applications (Knox et al., 2017; Miao et al., 2016; Roberts et al., 2018).

Twisted intramolecular charge transfer (TICT) is an electron transfer process that commonly occurs in molecules consisting of an electron donor-acceptor (D-A) pair linked by a single bond (Drummen, 2012; Sasaki et al., 2016). Upon photoexcitation, molecules in the TICT state returns to the ground state through red-shifted emission and enhanced nonradiative relaxation, which is usually accompanied by a strong PA signal output. The TICT effect can be easily tuned by modulation of substituents and configuration of D-A moieties, which makes the TICT effect an ideal strategy for activatable sensors (Hirayama et al., 2013; Reja et al., 2016; Ren et al., 2016). On the other hand, the aggregation-induced emission (AIE) phenomenon, a concept firstly coined in 2001 by Tang group, is another widely adopted strategy to design stimuli-responsive sensors since the optical properties of AIE luminogens (AIEgens) are potentially environment-dependent (Gao and Tang, 2017; Wang and Tang, 2019; Xu et al., 2020a). AIEgens commonly show enhanced emission in the aggregated state, which is mainly attributed to the restriction of intramolecular motions. AIEgens have made great contributions to bioimaging applications, especially those in the

[1]Center for AIE Research, College of Materials Science and Engineering, Shenzhen University, Shenzhen 518060, P. R. China

[2]Key Laboratory of Optoelectronic Devices and Systems of Ministry of Education and Guangdong Province, College of Physics and Optoelectronic Engineering, Shenzhen University, Shenzhen 518060, P. R. China

[3]Department of Chemistry, Hong Kong Branch of Chinese National Engineering Research Center for Tissue Restoration and Reconstruction, The Hong Kong University of Science and Technology, Clear Water Bay, Kowloon, Hong Kong 999077, P. R. China

[4]Key Laboratory of Molecular Target & Clinical Pharmacology and the State Key Laboratory of Respiratory Disease, School of Pharmaceutical Sciences, Guangzhou Medical University, Guangzhou 511436, P. R. China

[5]These authors contributed equally

[6]Lead contact

*Correspondence: liyingway@szu.edu.cn (Y.L.), wangd@szu.edu.cn (D.W.), tangbenz@ust.hk (B.Z.T.)

https://doi.org/10.1016/j.isci.2021.102261

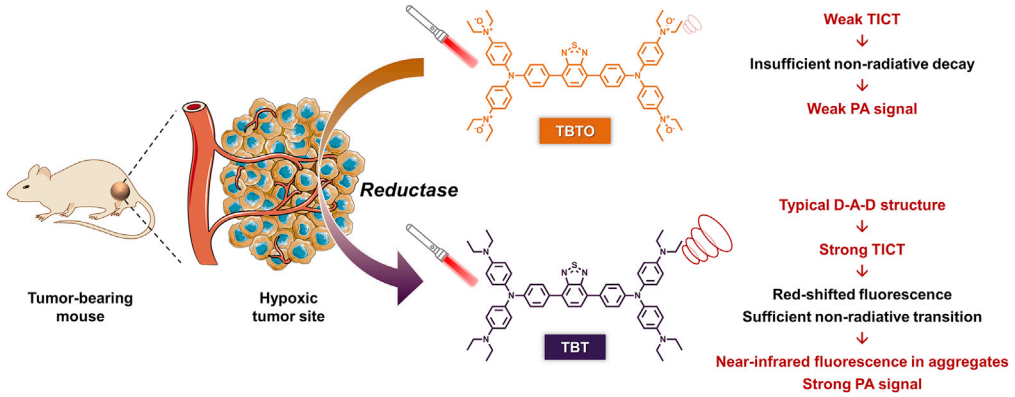

Scheme 1. Schematic illustration of hypoxia-activated probe for NIR fluorescence and photoacoustic dual-mode tumor imaging

Hypoxia probe TBTO undergoes reduction reaction by reductase, such as CYP450 enzymes in the hypoxic tumor site, to produce TBT, which shows red-shifted fluorescence and enhanced PA signal due to the strong TICT effect.

near-infrared (NIR) window, by regulating multi-hierarchical structures from single-molecule to molecular aggregates (Liu et al., 2020; Xu et al., 2020b; Zhang et al., 2020; Zhao et al., 2020). AIE effect endows molecules with high fluorescence efficiency while the TICT effect enables a red-shifted emission and enhanced non-radiative relaxation (Li et al., 2015, 2017). By molecular engineering in terms of adjusting the balance between TICT and AIE processes, fluorophores with NIR emission and excellent PA behavior can be obtained for NIR fluorescence and PA dual-mode imaging in deep tissue (Li et al., 2020c; Liu et al., 2019). However, the construction of stimuli-activated fluorophores that show turn-on NIR emission and PA signal triggered by the specific microenvironment *in vivo* is an appealing yet significantly challenging task (Li et al., 2018, 2020a; Meng et al., 2018).

Herein, we rationally designed and synthesized a hypoxia-responsive probe TBTO (Triphenylamine-Benzothiadiazole-Triphenylamine derivative featuring four diethylamino *N*-oxide groups) that could undergo bioreduction in a hypoxic microenvironment, producing TBT with a typical D-A-D structure. It was demonstrated that TBT possesses NIR fluorescence emission and PA signal generation, benefiting from its both AIE property and a strong TICT effect. *In vitro* and *in vivo* assessments revealed the responsiveness of TBTO in a reductive environment and its NIR fluorescence and PA dual-mode imaging ability.

RESULTS

Design and synthesis of TBT and TBTO

The design of the hypoxia probe TBTO was based on previous reports demonstrating that the dimethylamino/diethylamino *N*-oxide group could be converted to dimethylamino/diethylamino group by reductases, such as cytochrome P450 (CYP450), over-produced in hypoxic regions of solid tumors (Albertella et al., 2008; Knox et al., 2017; Nishida et al., 2010). The synthetic route of TBTO is shown in Scheme S1 and all the products are fully characterized by nuclear magnetic resonance spectroscopy (NMR) and high-resolution mass spectra (See supplemental information for experimental details, Figures S1–S8). TBT with four diethylamino groups was firstly synthesized in a few steps with a high yield, and then the oxidation of TBT by *m*-chloroperbenzoic acid (*m*-CPBA) afforded TBTO having four diethylamino *N*-oxide groups.

As illustrated in Scheme 1, we assume that TBTO could be converted to TBT by the reductases over-produced in the hypoxic tumor site. TBT has a typical D-A-D structure resulting from its inherent constituents including two triphenylamine fragments modified with diethylamino substituents acting as electron-donating units and a 2,1,3-benzothiadiazole group serving as an electron-accepting moiety. TICT is a common phenomenon in a molecule consisting of a D-A pair linked by a single bond (Scheme S2). In a polar environment such as the aqueous media in the biosystem, upon photoexcitation, such molecules undergo fast intramolecular electron transfer, accompanied by D-A twisting of the single bond. As a result, the locally excited state equilibrates rapidly with the TICT state with lower energy and subsequently returns

Table 1. Photophysical properties of TBTO and TBT

Compound	ε ($M^{-1}\cdot cm^{-1}$)[a]	$\lambda_{abs,\ max}$[a]	$\lambda_{em,\ max}$[a]	$\lambda_{em,\ max}$[b]	QY[a]	QY[b]
TBTO	0.7×10^4	450 nm	592 nm	600 nm	69%	8.2%
TBT	1.8×10^4	530 nm	Undetectable	740 nm	0.2%	5.7%

[a]in THF solution.
[b]in the solid state.

to the ground state with a red-shifted emission. Additionally, the susceptibility of the TICT state favors multiple nonradiative quenching process, leading to a severely impaired fluorescence efficiency and enhanced PA signal output. In contrast, as for TBTO, the oxidation state of diethylamino decreases the electron-donating property of the nitrogen atom and prevents its lone pair from participating in the TPA conjugation system, leading to a much weaker TICT effect. Thus, TBTO would have a blue-shifted fluorescence emission and neglectable PA signal (Scheme 1).

Photophysical properties of TBT and TBTO

The introduction of electron-donating groups to a D-A effect featured fluorophore usually leads to red-shifted absorption and fluorescence emission. Indeed, as shown in Table 1, TBTO had an absorption maximum at 450 nm in tetrahydrofuran (THF) solution while the absorption of TBT centered at 530 nm. In the solid state, the emission maxima of TBTO and TBT were determined to be 600 and 740 nm, respectively. To have a better understanding of the above phenomenon, density functional theory (DFT) calculations were conducted at the B3LYP/6-31+G(d) level (Figure 1). Due to the strong electron-donating ability of the diethylamino group as compared to its oxidized form, the frontier molecular orbitals (both HOMO and LUMO) of TBT are more delocalized as compared to those of TBTO, leading to elevated HOMO and LUMO energy levels (Mao et al., 2018). Moreover, TBT possesses a much smaller HOMO-LUMO energy gap than TBTO, which is well consistent with the experimental data depicted in Table 1 that TBT has a red-shifted absorption and emission.

To compare their TICT behavior, we evaluated the solvatochromic property of each compound by using a variety of solvents including two non-polar solvents (hexane and toluene), two less polar solvents (THF and ethyl acetate), and two polar solvents (dimethylformamide and methanol) (polarity: hexane < toluene << THF ~ ethyl acetate < dimethylformamide < methanol). As depicted in Figure 2D, TBT was only emissive in hexane and toluene, and the fluorescence in polar solvents is not detectable under the same measurement conditions. Besides, the maximum emission of TBT red shifted from 637 nm to 700 nm when changing the solvent from hexane to toluene (Figure S9D). The obvious fluorescence quenching and red-shift with the increasing solvent polarity solidly indicated the strong TICT effect of TBT. It's worth mentioning that there is no obvious shift of the absorption spectra of TBT in different solvents (Figure S9C), suggesting that the above solvatochromic behavior was not caused by the difference of light-harvesting. Since TBTO is not soluble in hexane and toluene, the fluorescence emission spectra in the other four solvents were recorded. As displayed in Figures 2A and S9B, TBTO was emissive in all the polar solvents. Although the fluorescence changes of TBTO were observed in terms of both emission wavelength and intensity upon altering solvent polarity, the tendency was not accordant with the expected outcomes of the TICT effect, presenting the non-TICT feature of TBTO.

Furthermore, the solvatochromic behavior of those two compounds was investigated in mixed solvent systems. In the case of THF-hexane mixtures, TBT showed gradually blue-shifted and enhanced fluorescence with the increasing of the fraction of hexane (Figures 2E and S10C); while TBTO exhibit a decreased emission with little shift (Figures 2B and S10A). In the case of THF-water mixtures, similar results were observed for TBTO (Figures 2C and S10B); while TBT displayed gradually red-shifted emission with the addition of water as a strong polar solvent (Figures 2F and S10D). These results are in full agreement with our assumption that TBT is a typical TICT molecule whereas TBTO is not. It is important to note that the fluorescence of TBT gradually enhanced with the increasing of the fraction of water, which could be ascribed to the AIE property of TBT. The fluorescence quantum yield (QY) values of TBT in THF solution (Φ_{FL} = 0.2%) and the solid state (Φ_{FL} = 5.7%) provided additional evidence for the AIE behavior of TBT (Table 1).

To gain insights into the non-radiative relaxation efficiency of TBT and TBTO, the photothermal conversion performance was estimated under the irradiation of a 660 nm laser at a power of 0.5 W/cm^2. As a result, the

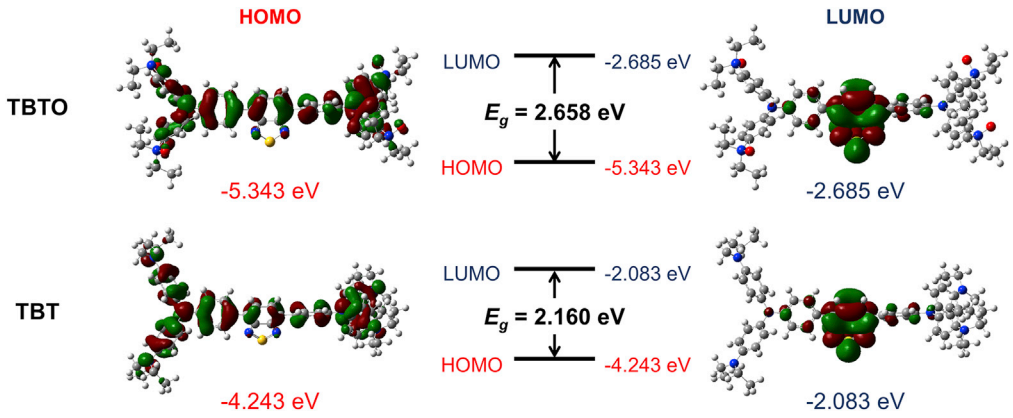

Figure 1. Density functional theory (DFT) calculations

Molecular orbital amplitude plots of the highest occupied molecular orbital (HOMO) and lowest unoccupied molecular orbital (LUMO) energy levels of TBTO and TBO calculated at the B3LYP/6-31+G(d) level.

temperature of TBT solution increased by 20°C within 3 min irradiation, whereas the TBTO solution maintained almost the same temperature (Figure S11). This revealed that TBT possesses a relatively high non-radiative relaxation efficiency, which is favorable for PA signal generation. Importantly, TBT has a higher molar extinction efficiency than TBTO (Table 1), which is also beneficial for PA imaging according to the literature reported (Borg and Rochford, 2018). All these results suggested the significant capacity of TBTO for potential PA and fluorescence dual-mode imaging, once exposed to a reductive environment.

Preparation and characterization of TBTO NPs and TBT NPs

Before testing the responsibility of TBTO to the reductive species, TBTO nanoparticles (TBTO NPs) were fabricated to improve the biocompatibility and dispersibility in aqueous solution by encapsulating TBTO with an amphiphilic co-polymer DSPE-mPEG2000 through a typical nanoprecipitation method. Dynamic light scattering measurement revealed that the average size of TBTO NPs is around 50 nm, which is in agreement with the transmission electron microscopy (TEM) image (Figure 3A, Table S1). Additionally, the Zeta potential of TBTO NPs was measured to be −23 mV (Table S1), and the negatively charged NPs are favorable for long blood circulation and resistant to non-specific interactions for *in vivo* analysis. TBTO NPs have a maximum absorption at 441 nm and maximum emission at 596 nm (Figure 3B). Moreover, TBT NPs were also prepared using the same protocol as above presenting an average size of 103 nm and Zeta potential of −41.2 mV (Figure S12, Table S1). TBT NPs have a maximum absorption at 542 nm and maximum emission at 724 nm (Figure 3B). The spectral separation of TBTO NPs and TBT NPs allows for selective detection of a signal from one compound without apparent interference from the other.

Responsibility of TBTO NPs to the reductive environment *in vitro*

Diethylamino *N*-oxide groups have previously been proven to be reduced by Fe(II), thus it is critical to determine the response of TBTO NPs to Fe(II) among different metal ions (Hirayama et al., 2013, 2017; Knox et al., 2017; Xu et al., 2019). To that end, TBTO NPs were incubated with various metal ions in PBS at 37°C and the fluorescence intensity at 600 nm with an excitation of 450 nm was measured every 5 min to monitor the consumption of TBTO (Figure S13). The fluorescence emission of TBTO was strongly quenched by 18 times with prolonging the incubation time to 30 min in the presence of 10 equivalents of Fe(II) (Figure 3C). As for other metal ions, no fluorescence change was detected. Furthermore, totally different optical spectra of TBTO NPs solution were observed with or without Fe(II) treatment (Figure S14), strongly suggesting the specific responsiveness of TBTO to reductive species. The transition of TBTO to TBT was verified by ^{1}H-NMR using Na_2SO_3 as the reductive agent (Figure S15).

We then sought to determine whether TBTO NPs could undergo the hypoxia-responsive fluorescence quenching at a cellular level before moving to *in vivo* studies. HeLa cells, a human cervical cancer cell line, were firstly cultured either under a standard atmosphere containing 20% oxygen (normoxic condition) or in a sealed container with an anaerobic gas generator to keep the oxygen level lower than 0.1% (hypoxic condition). After pre-incubation for 12 h in the above conditions, cells were treated with 50 μM TBTO NPs

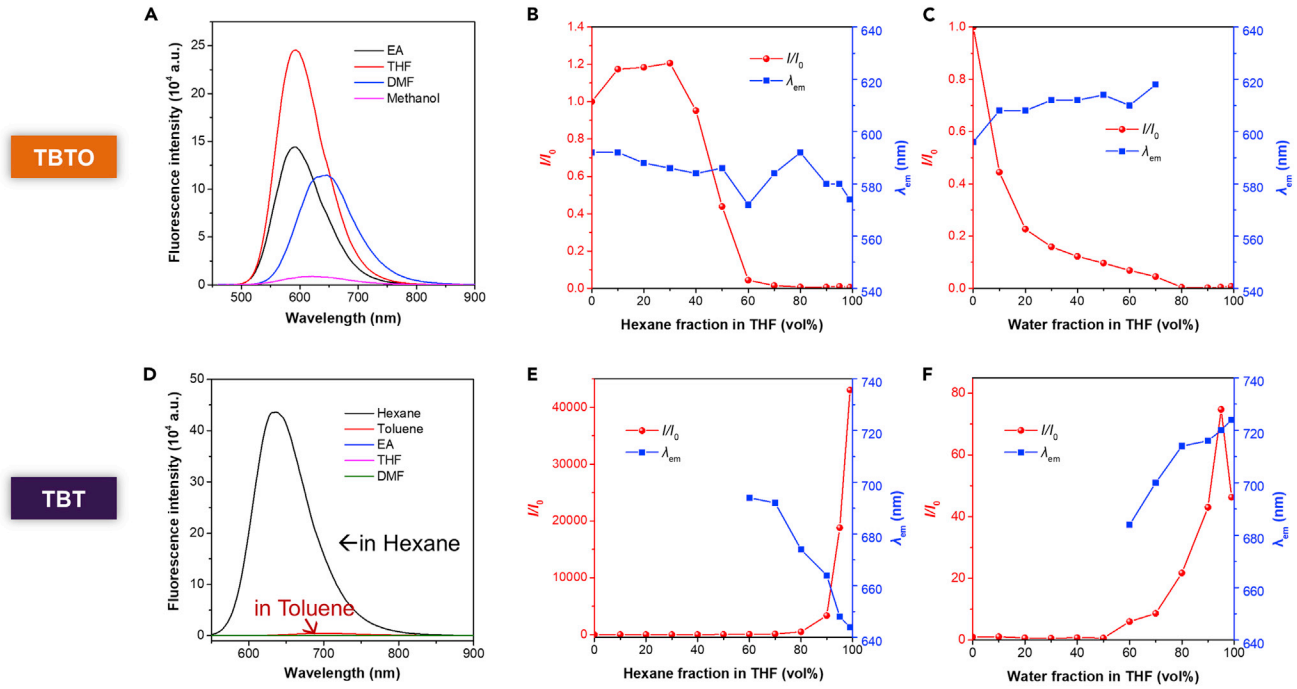

Figure 2. Solvatochromic effect of TBT and TBTO in different solvents

(A and D) Fluorescence emission spectra of (A) TBTO and (D) TBT in different solvents. [TBTO], [TBT] = 20 μM.

(B and E) Fluorescence emission changes of (B) TBTO and (E) TBT in THF with different fractions of hexane (red curve: the fluorescence intensity ratio I/I_0 in the function of hexane fraction, I_0 indicates the fluorescence intensity in pure THF; blue curve: the maximum emission wavelength in the function of hexane fraction). [TBTO], [TBT] = 20 μM.

(C and F) Fluorescence emission changes of (C) TBTO and (F) TBT in THF with different fractions of water (red curve: the fluorescence intensity ratio I/I_0 in the function of water fraction, I_0 indicates the fluorescence intensity in pure THF; blue curve: the maximum emission wavelength in the function of water fraction). [TBTO], [TBT] = 20 μM.

and then a further incubation for 3 h under normoxic or hypoxic conditions. After that, the fluorescence intensities at 600 nm (λ_{ex}: 450 nm) of the cell culture supernatants were measured in a microplate reader. As compared to the normoxic conditions, TBTO NPs suffered from a much stronger fluorescence quenching in the cells cultured in hypoxic conditions (Figure 3D). These outcomes revealed the efficient responsiveness of TBTO NPs to the reductive environment of cells cultured under hypoxia. The colocalization experiments performed with different organelle trackers indicated that TBTO NPs were mostly located in lipid droplets (Figure S16). It is worth mentioning that neither TBTO nor TBT exhibited cytotoxicity to HeLa cells at a concentration up to 100 μM indicating the biocompatibility of TBTO as a hypoxia probe (Figure S17).

Hypoxia-responsive NIR fluorescence imaging of TBTO NPs *in vivo*

Encouraged by the *in vitro* hypoxia-responsibility of TBTO NPs, we subsequently investigated hypoxia-activated NIR imaging in tumor-bearing mice. Tumor allografts were constructed via subcutaneous implantation of HeLa cells into BALB/c mice. To monitor the conversion of TBTO to TBT in real-time, two mice were administered TBTO NPs (Figure 4A) and TBT NPs (Figure 4C) via intratumoral injection, respectively. Both mice were transferred to the small animal imaging system and imaged with excitation filters of 500 nm and 570 nm and corresponding NIR emission filters of 720 and 740 nm after different time intervals post-injection. As illustrated in Figures 4A and 4B, for the mouse injected with TBTO NPs, the fluorescence signal collected with the excitation filter of 500 nm gradually decreased, whereas the signal from 570 nm excitation gradually increased, demonstrating that TBTO underwent a reduction reaction in the hypoxic tumor. TBT NPs injected mouse, on the other hand, exhibited almost constant NIR fluorescence intensities within 100 min post-injection upon excitation with either 500 nm or 570 nm (Figures 4C and 4D), because TBT is inactive to the tumorous microenvironment. Since a shorter wavelength impedes the penetration in deep tissue, using a longer excitation wavelength never goes wrong for *in vivo* NIR imaging. The transition process was further reproduced using more mice (Figure S18). Moreover, the good photostability of TBTO NPs

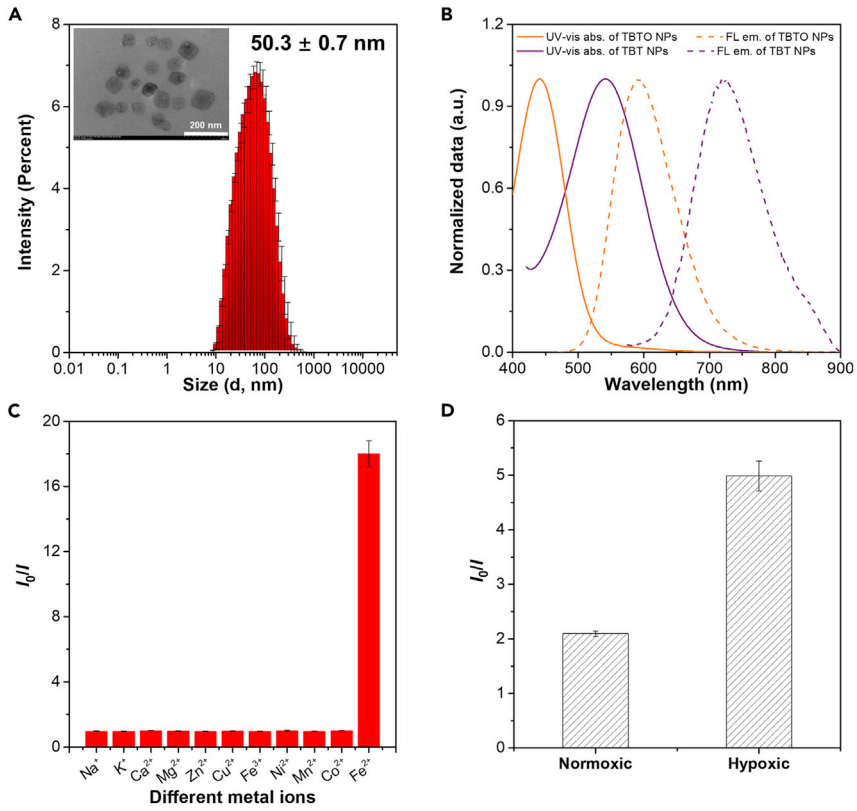

Figure 3. Characterization of TBTO NPs and TBT NPs, and *in vitro* responsiveness of TBTO NPs to reductive environment

(A) Size distribution of TBTO NPs. Insert picture: TEM image of TBTO NPs. Data are represented as mean ± SD from three replicates.

(B) Normalized absorption and emission spectra of TBTO NPs and TBT NPs.

(C) Fluorescence responses of TBTO NPs (50 μM) to different metal ions (500 μM) in PBS buffer (pH 7.4) after 30 min incubation. Data are represented as mean ± SD from three replicates.

(D) Fluorescence responses of TBTO NPs to different culture conditions (normoxic or hypoxic) of HeLa cells. Data are represented as mean ± SD from three replicates.

and TBT NPs was confirmed using the small animal imaging system (Figure S19). Thus, we could conclude that TBTO is promising as a hypoxia-activated NIR imaging agent. We next examined the tumor-targeting specificity and persistence of TBTO NPs via tail intravenous injection. As shown in Figures S20A and S20B, at 6 h post-injection, an obvious NIR fluorescence signal upon 570 nm excitation was detected in tumor and the intensity persisted more than 24 h. *Ex vivo* images of major organs and tumors at the time point of 24 h post-injection further verified the remarkable accumulation of TBTO NPs in tumors (Figure S20C). *Ex vivo* colocalization of TBTO signal in tumor site with a commercial hypoxia imaging kit via an immunofluorescence staining method was illustrated in Figure S21 (see supplemental information for experimental details).

PA imaging of TBTO NPs *in vivo*

In the primary test, PA signals of both TBTO and TBT solutions were tested. As illustrated in Figure 5A, TBT showed a fairly strong PA signal whereas almost no PA signal was detected from TBTO under the same experimental conditions. We also performed *in vitro* PA imaging of TBTO NPs and TBT NPs aqueous solution (1 mg/mL) in fluorinated ethylene propylene tubes which were inserted into the tissue-mimicking phantom (Figure S22). In addition, PA signal of TBT could be detected *in vivo* upon intravenous administration of TBT NPs in tumor-bearing mice (Figure S23). These results suggested that TBTO can be potentially utilized as a hypoxia-triggered PA imaging agent with turn-on characteristics. To verify that, TBTO NPs were administered to tumor-bearing mice intravenously via tail vein injection, and *in vivo* PA images

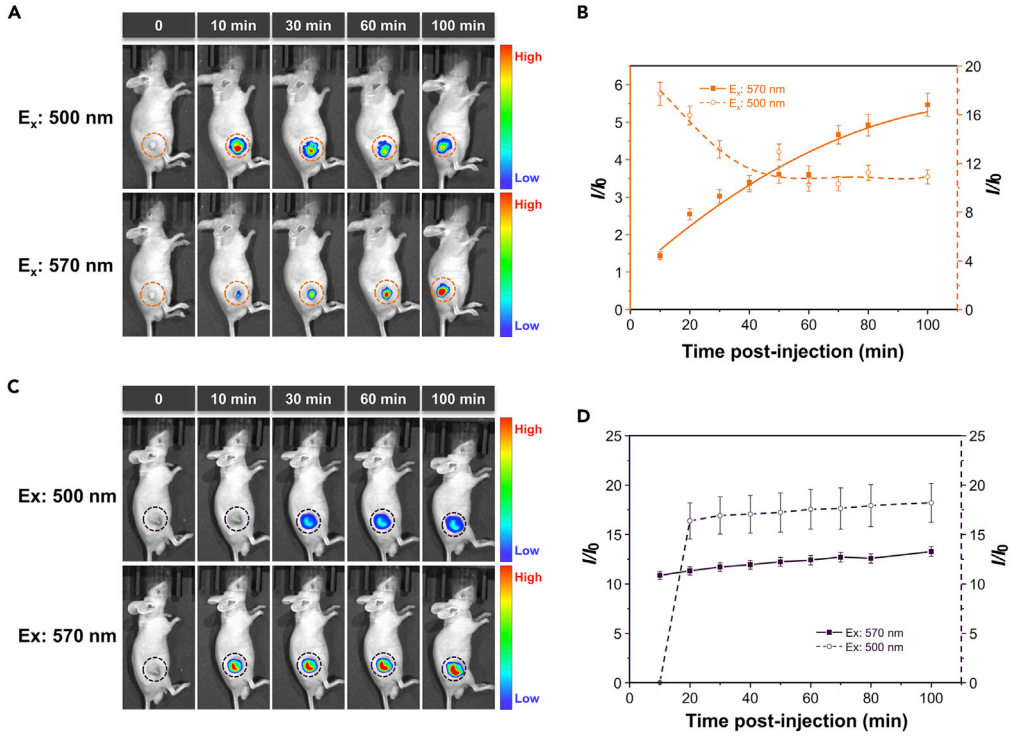

Figure 4. Hypoxia-activated NIR fluorescence imaging of TBTO NPs *in vivo*

(A and C) Time-lapse NIR fluorescence imaging of mice before (time point: 0 min) and after intratumoral injection with (A) TBTO NPs and (C) TBT NPs (50 μL, 1 mg/mL), respectively. The fluorescence signals were collected upon excitation with 500 nm and 570 nm, respectively.

(B and D) Semiquantitative analysis of fluorescence intensities in the tumor site of the mouse injected with (B) TBTO NPs and (D) TBT NPs as a function of time. Data are represented as mean ± SD from three replicates.

were acquired at 6 h, 1 d, 2 d, and 3 d following injection (Figure 5B). Semiquantitative analysis of average PA intensities in the tumor site at different time points was also performed (Figure 5C). It was observed that a strong PA signal was detected after 6 h post-injection resulting from the responsiveness of TBTO to hypoxia. Even after 3 days, the PA signal could still be detected, suggesting the utility of TBTO NPs for long-term tracking of the tumor.

Lastly, we evaluated the physiological clearance of TBTO NPs from mice, which is highly related to the biosafety for *in vivo* applications. As depicted in Figure S24A, upon intravenous injection of TBTO NPs via the tail vein, TBTO NPs could be eliminated from all major organs within 72 h. In the case of intratumoral injection, there were no PA signals detected in major organs after 48 h, and the PA signal in the tumor site was clearly presented with high contrast and then slowly cleared out until 72 h (Figure S24B). H&E staining results of the major organs (heart, liver, spleen, lung, and kidney) indicated the good biosafety and biocompatibility of TBT NPs and TBTO NPs (Figure S25). We could conclude from all these results that TBTO NPs is significantly promising for long-term tumor imaging as a hypoxia-activated PA probe with appropriate biocompatibility.

DISCUSSION

In summary, we rationally designed a hypoxia-activable probe TBTO, which is capable of being converted to AIE-active TBT in a hypoxic microenvironment. TBTO could be facilely synthesized in a few steps with a high yield. The typical D-A-D structure of TBT led to a strong TICT effect, which red-shifted the fluorescence emission to the NIR region and promoted the generation of PA signal. The fluorescence emission of TBT exhibited a positive solvatochromic effect with a bathochromic shift and quenched emission along with the increasing of solvent polarity, indicating a typical TICT phenomenon. The conversion of TBTO to TBT in a reductive environment was confirmed by fluorescence spectra and ^{1}H-NMR. *In vitro* responsiveness of

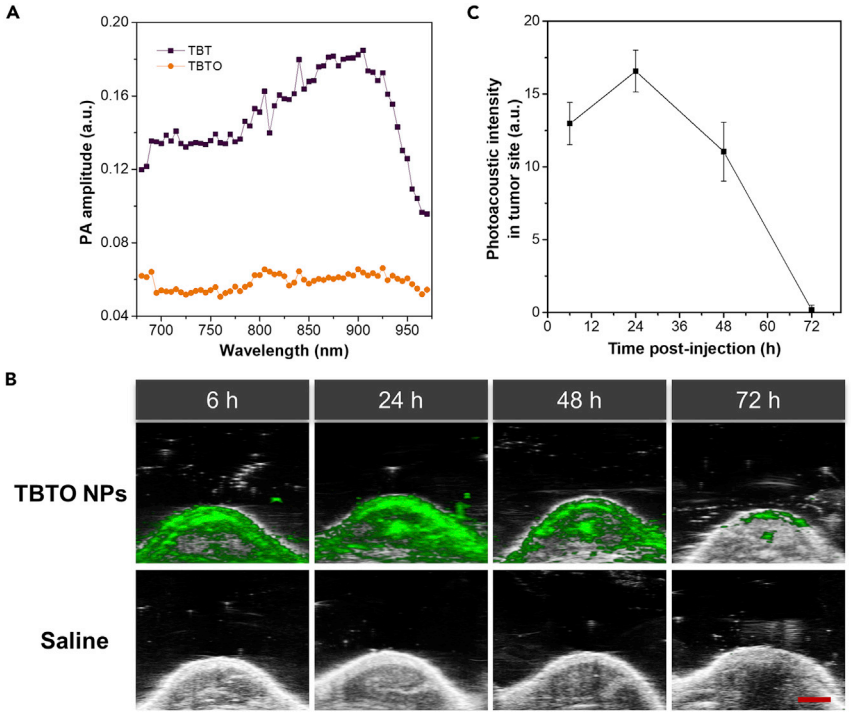

Figure 5. Hypoxia-activated PA Imaging of TBTO NPs

(A) *In vitro* PA spectra of TBTO and TBT. PA amplitude corresponding to each compound was plotted as a function of wavelength.

(B) *In vivo* PA images of the tumor site in the mice after tail intravenous injection with TBTO NPs (200 μL, 1 mg/mL) or saline (200 μL) as control. Scale bar represents 2 mm.

(C) Semiquantitative analysis of average PA intensities in the tumor site of the mice injected with TBTO NPs as a function of time. Data are represented as mean ± SD from three replicates.

TBTO in hypoxic cells was confirmed by monitoring the fluorescence quenching of TBTO signal. *In vivo* assessments revealed that TBTO with good biocompatibility was highly responsive to the hypoxic tumor and well-performed in NIR fluorescence and PA dual-mode tumor imaging. This work presents a promising method for clinical imaging taking advantage of the specific microenvironment in a diseased region, which might be useful in tumor diagnostics, imaging-guided surgical interventions, and treatment efficacy evaluations.

Limitations of the study

We have presented a hypoxia-responsive probe TBTO allowing for NIR-I imaging and more importantly PA imaging in solid tumors. Although the fluorescence emission could cover the NIR-I area, NIR-II fluorophores featuring longer absorption and emission wavelengths are worth investigating in the future for hypoxia imaging in deep tissue with high resolution (Li et al., 2020b; Sun et al., 2019; Tu et al., 2019; Xu et al., 2020c).

Resource availability

Lead contact

Further information and requests for reagents and resources should be directed to and will be fulfilled by the lead contact, Ben Zhong Tang (tangbenz@ust.hk).

Materials availability

All unique reagents generated in this study are available from the lead contact with a completed Materials Transfer Agreement.

Data and code availability

The published article includes all datasets generated or analyzed during the study.

METHODS

All methods can be found in the accompanying transparent methods supplemental file.

SUPPLEMENTAL INFORMATION

Supplemental information can be found online at https://doi.org/10.1016/j.isci.2021.102261.

ACKNOWLEDGMENTS

This work was partially supported by the China Postdoctoral Science Foundatio (2020M672813, 2019M653003), the National Science Foundation for Distinguished Young Scholars of Guangdong Province (2020B1515020011), the National Natural Science Foundation of China (21801169), and the Science and Technology Foundation of Shenzhen City (JCYJ20190808153415062, JCYJ20200109110608167). The authors also acknowledge the Instrumental Analysis Center of Shenzhen University.

AUTHOR CONTRIBUTIONS

M. L. and D. W. conceived the idea and designed the experiments. M. L. synthesized and characterized all the materials. Q. W. performed the theoretical calculations. M. L. tested the *in vitro* responses of TBTO NPs. M. L., N. N., J. H., and Y. L. performed the *in vivo* fluorescence imaging in tumor-bearing mice. H. L., L. Z., and Y. L. performed the *in vivo* PA imaging in tumor-bearing mice. M. L. and D. W. wrote the manuscript. All the authors discussed the results and commented on the manuscript. D. W., and B. Z. T. supervised the overall research.

DECLARATION OF INTERESTS

The authors declare no conflict of interest.

Received: November 30, 2020
Revised: February 13, 2021
Accepted: February 25, 2021
Published: March 19, 2021

REFERENCES

Albertella, M.R., Loadman, P.M., Jones, P.H., Phillips, R.M., Rampling, R., Burnet, N., Alcock, C., Anthoney, A., Vjaters, E., Dunk, C.R., et al. (2008). Hypoxia-selective targeting by the bioreductive prodrug AQ4N in patients with solid tumors: results of a phase i study. Clin. Cancer Res. *14*, 1096–1104.

Borg, R.E., and Rochford, J. (2018). Molecular photoacoustic contrast agents: design principles & applications. Photochem. Photobiol. *94*, 1175–1209.

Brown, J.M., and Wilson, W.R. (2004). Exploiting tumour hypoxia in cancer treatment. Nat. Rev. Cancer *4*, 437–447.

Drummen, G.P. (2012). Fluorescent probes and fluorescence (microscopy) techniques–illuminating biological and biomedical research. Molecules *17*, 14067–14090.

Gao, M., and Tang, B.Z. (2017). Fluorescent sensors based on aggregation-induced emission: recent advances and perspectives. ACS Sensors *2*, 1382–1399.

Hai, P., Imai, T., Xu, S., Zhang, R., Aft, R.L., Zou, J., and Wang, L.V. (2019). High-throughput, label-free, single-cell photoacoustic microscopy of intratumoral metabolic heterogeneity. Nat. Biomed. Eng. *3*, 381–391.

Harris, A.L. (2002). Hypoxia — a key regulatory factor in tumour growth. Nat. Rev. Cancer *2*, 38–47.

Hirayama, T., Okuda, K., and Nagasawa, H. (2013). A highly selective turn-on fluorescent probe for iron(ii) to visualize labile iron in living cells. Chem. Sci. *4*, 1250–1256.

Hirayama, T., Tsuboi, H., Niwa, M., Miki, A., Kadota, S., Ikeshita, Y., Okuda, K., and Nagasawa, H. (2017). A universal fluorogenic switch for Fe(II) ion based on *N*-oxide chemistry permits the visualization of intracellular redox equilibrium shift towards labile iron in hypoxic tumor cells. Chem. Sci. *8*, 4858–4866.

Knox, H.J., and Chan, J. (2018). Acoustogenic probes: a new frontier in photoacoustic imaging. Acc. Chem. Res. *51*, 2897–2905.

Knox, H.J., Hedhli, J., Kim, T.W., Khalili, K., Dobrucki, L.W., and Chan, J. (2017). A bioreducible *N*-oxide-based probe for photoacoustic imaging of hypoxia. Nat. Commun. *8*, 1794–1802.

Li, B., Lu, L., Zhao, M., Lei, Z., and Zhang, F. (2018). An efficient 1064 nm NIR-II excitation fluorescent molecular dye for deep-tissue high-resolution dynamic bioimaging. Angew. Chem. Int. Ed. *57*, 7483–7487.

Li, B., Zhao, M., Feng, L., Dou, C., Ding, S., Zhou, G., Lu, L., Zhang, H., Chen, F., Li, X., et al. (2020a). Organic NIR-II molecule with long blood half-life for in vivo dynamic vascular imaging. Nat. Commun. *11*, 3102.

Li, J., Liu, Y., Xu, Y., Li, L., Sun, Y., and Huang, W. (2020b). Recent advances in the development of NIR-II organic emitters for biomedicine. Coord. Chem. Rev. *415*, 213318.

Li, J., Qian, Y., Xie, L., Yi, Y., Li, W., and Huang, W. (2015). From dark TICT state to emissive quasi-TICT state: the AIE mechanism of n-(3-(benzo[d] oxazol-2-yl)phenyl)-4-tert-butylbenzamide. J.Phys. Chem. C *119*, 2133–2141.

Li, K., Liu, Y.Y., Li, Y.Y., Feng, Q., Hou, H.W., and Tang, B.Z. (2017). 2,5-bis(4-alkoxycarbonylphenyl)-1,4-diaryl-1,4-

dihydropyrrolo[3,2-b]pyrrole (AAPP) AIEgens: tunable RIR and TICT characteristics and their multifunctional applications. Chem. Sci. *8*, 7258–7267.

Li, Y., Cai, Z., Liu, S., Zhang, H., Wong, S.T.H., Lam, J.W.Y., Kwok, R.T.K., Qian, J., and Tang, B.Z. (2020c). Design of AIEgens for near-infrared IIb imaging through structural modulation at molecular and morphological levels. Nat. Commun. *11*, 1255–1264.

Liu, J.-n., Bu, W., and Shi, J. (2017). Chemical design and synthesis of functionalized probes for imaging and treating tumor hypoxia. Chem. Rev. *117*, 6160–6224.

Liu, S., Li, Y., Kwok, R.T.K., Lam, J.W.Y., and Tang, B.Z. (2020). Structural and process controls of AIEgens for NIR-II theranostics. Chem. Sci. https://doi.org/10.1039/d0sc02911d.

Liu, S., Zhou, X., Zhang, H., Ou, H., Lam, J.W.Y., Liu, Y., Shi, L., Ding, D., and Tang, B.Z. (2019). Molecular motion in aggregates: manipulating TICT for boosting photothermal theranostics. J. Am. Chem. Soc. *141*, 5359–5368.

Liu, Y.J., Nie, L.M., and Chen, X.Y. (2016). Photoacoustic molecular imaging: from multiscale biomedical applications towards early-stage theranostics. Trends Biotechnol. *34*, 420–433.

Mallidi, S., Luke, G.P., and Emelianov, S. (2011). Photoacoustic imaging in cancer detection, diagnosis, and treatment guidance. Trends Biotechnol. *29*, 213–221.

Mao, Y., Head-Gordon, M., and Shao, Y. (2018). Unraveling substituent effects on frontier orbitals of conjugated molecules using an absolutely localized molecular orbital based analysis. Chem. Sci. *9*, 8598–8607.

Meng, X., Zhang, J., Sun, Z., Zhou, L., Deng, G., Li, S., Li, W., Gong, P., and Cai, L. (2018). Hypoxia-triggered single molecule probe for high-contrast NIR II/PA tumor imaging and robust photothermal therapy. Theranostics *8*, 6025–6034.

Miao, Q.Q., Lyu, Y., Ding, D., and Pu, K.Y. (2016). Semiconducting oligomer nanoparticles as an activatable photoacoustic probe with amplified brightness for in vivo imaging of pH. Adv. Mater. *28*, 3662–3668.

Nishida, C.R., Lee, M., and de Montellano, P.R.O. (2010). Efficient hypoxic activation of the anticancer agent AQ4N by CYP2S1 and CYP2W1. Mol. Pharmacol. *78*, 497–502.

Ou, H., Li, J., Chen, C., Gao, H., Xue, X., and Ding, D. (2019). Organic/polymer photothermal nanoagents for photoacoustic imaging and photothermal therapy in vivo. Sci. China Mater. *62*, 1740–1758.

Rankin, E.B., Nam, J.M., and Giaccia, A.J. (2016). Hypoxia: signaling the metastatic cascade. Trends Cancer *2*, 295–304.

Reja, S.I., Khan, I.A., Bhalla, V., and Kumar, M. (2016). A TICT based NIR-fluorescent probe for human serum albumin: a pre-clinical diagnosis in blood serum. Chem. Commun. *52*, 1182–1185.

Ren, M., Deng, B., Kong, X., Zhou, K., Liu, K., Xu, G., and Lin, W. (2016). A TICT-based fluorescent probe for rapid and specific detection of hydrogen sulfide and its bio-imaging applications. Chem. Commun. *52*, 6415–6418.

Rey, S., Schito, L., Wouters, B.G., Eliasof, S., and Kerbel, R.S. (2017). Targeting hypoxia-inducible factors for antiangiogenic cancer therapy. Trends Cancer *3*, 529–541.

Roberts, S., Seeger, M., Jiang, Y., Mishra, A., Sigmund, F., Stelzl, A., Lauri, A., Symvoulidis, P., Rolbieski, H., Preller, M., et al. (2018). Calcium sensor for photoacoustic imaging. J. Am. Chem. Soc. *140*, 2718–2721.

Sasaki, S., Drummen, G.P.C., and Konishi, G.-i. (2016). Recent advances in twisted intramolecular charge transfer (TICT) fluorescence and related phenomena in materials chemistry. J. Mater. Chem. C *4*, 2731–2743.

Sun, Y., Ding, F., Chen, Z., Zhang, R., Li, C., Xu, Y., Zhang, Y., Ni, R., Li, X., Yang, G., et al. (2019). Melanin-dot–mediated delivery of metallacycle for NIR-II/photoacoustic dual-modal imaging-guided chemo-photothermal synergistic therapy. Proc. Natl. Acad. Sci. U S A *116*, 16729–16735.

Tu, L., Xu, Y., Ouyang, Q., Li, X., and Sun, Y. (2019). Recent advances on small-molecule fluorophores with emission beyond 1000 nm for better molecular imaging in vivo. Chin. Chem. Lett. *30*, 1731–1737.

Wang, D., and Tang, B.Z. (2019). Aggregation-induced emission luminogens for activity-based sensing. Acc. Chem. Res. *52*, 2559–2570.

Wang, L., Maslov, K., and Wang, L.V. (2013). Single-cell label-free photoacoustic flowoxigraphy in vivo. P. Natl. Acad. Sci. U S A *110*, 5759.

Weber, J., Beard, P.C., and Bohndiek, S.E. (2016). Contrast agents for molecular photoacoustic imaging. Nat. Methods *13*, 639–650.

Wong, T.T.W., Zhang, R., Zhang, C., Hsu, H.-C., Maslov, K.I., Wang, L., Shi, J., Chen, R., Shung, K.K., Zhou, Q., et al. (2017). Label-free automated three-dimensional imaging of whole organs by microtomy-assisted photoacoustic microscopy. Nat. Commun. *8*, 1386.

Xu, C.H., Zou, H., Zhao, Z., Zhang, P.F., Kwok, R.T.K., Lam, J.W.Y., Sung, H.H.Y., Williams, I.D., and Tang, B. (2019). A new strategy toward "simple" water-soluble aie probes for hypoxia detection. Adv. Funct. Mater. *29*, 1903278.

Xu, S.D., Duan, Y.K., and Liu, B. (2020a). Precise molecular design for high-performance luminogens with aggregation-induced emission. Adv. Mater. *32*, 1903530.

Xu, W., Wang, D., and Tang, B.Z. (2020b). NIR-II AIEgens: a win-win integration towards bioapplications. Angew. Chem. Int. Ed. https://doi.org/10.1002/anie.202005899.

Xu, Y., Zhang, Y., Li, J., An, J., Li, C., Bai, S., Sharma, A., Deng, G., Kim, J.S., and Sun, Y. (2020c). NIR-II emissive multifunctional AIEgen with single laser-activated synergistic photodynamic/photothermal therapy of cancers and pathogens. Biomaterials *259*, 120315.

Yao, J., Wang, L., Yang, J.-M., Maslov, K.I., Wong, T.T.W., Li, L., Huang, C.-H., Zou, J., and Wang, L.V. (2015). High-speed label-free functional photoacoustic microscopy of mouse brain in action. Nat. Methods *12*, 407–410.

Zhang, G., Palmer, G.M., Dewhirst, M.W., and Fraser, C.L. (2009). A dual-emissive-materials design concept enables tumour hypoxia imaging. Nat. Mater. *8*, 747–751.

Zhang, Q., Yu, P., Fan, Y., Sun, C., He, H., Liu, X., Lu, L., Zhao, M., Zhang, H., and Zhang, F. (2020). Bright and stable NIR-II J-aggregated AIE dibodipy-based fluorescent probe for dynamic in vivo bioimaging. Angew. Chem. Int. Ed. https://doi.org/10.1002/anie.202012427.

Zhao, M., Wang, J., Lei, Z., Lu, L., Wang, S., Zhang, H., Li, B., and Zhang, F. (2020). NIR-II pH sensor with a FRET adjustable transition point for in situ dynamic tumor microenvironment visualization. Angew. Chem. Int. Ed. https://doi.org/10.1002/anie.202012021.

iScience, Volume *24*

Supplemental information

Hypoxia-activated probe for NIR fluorescence and photoacoustic dual-mode tumor imaging

Meng Li, Huan Li, Qian Wu, Niu Niu, Jiachang Huang, Lingmin Zhang, Ying Li, Dong Wang, and Ben Zhong Tang

Supplemental Data

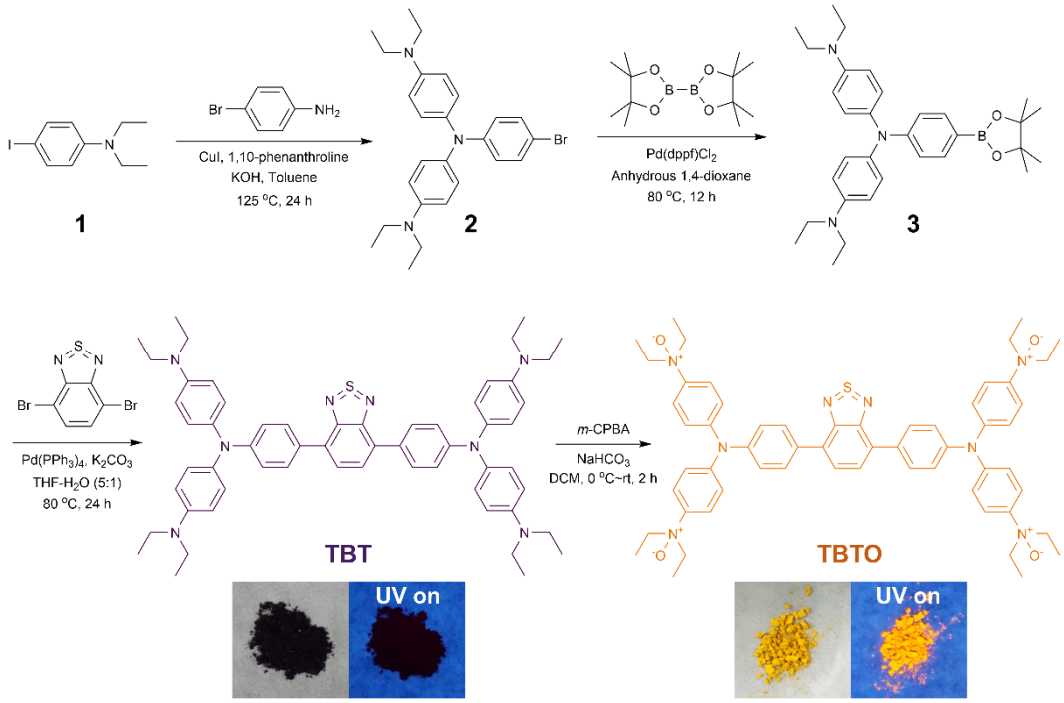

Scheme S1. Synthetic Route of TBT and TBTO, Related to Scheme 1.

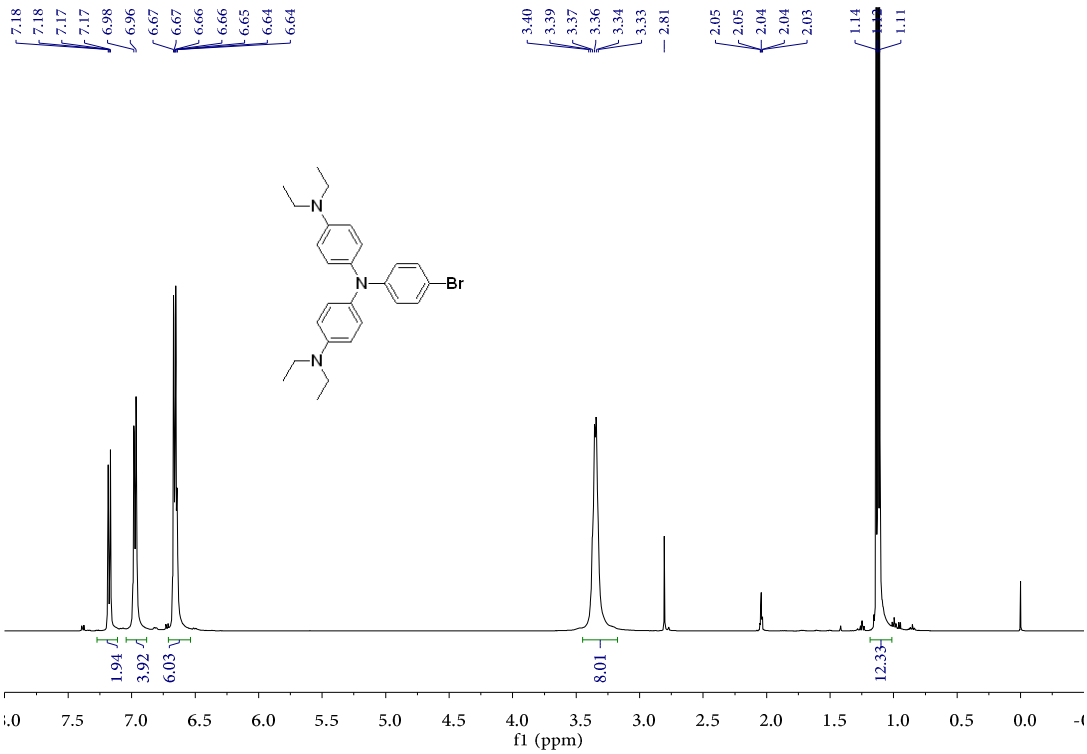

Figure S1. ^{1}H-NMR of Compound 2 in d_6-Acetone, Related to Scheme 1.

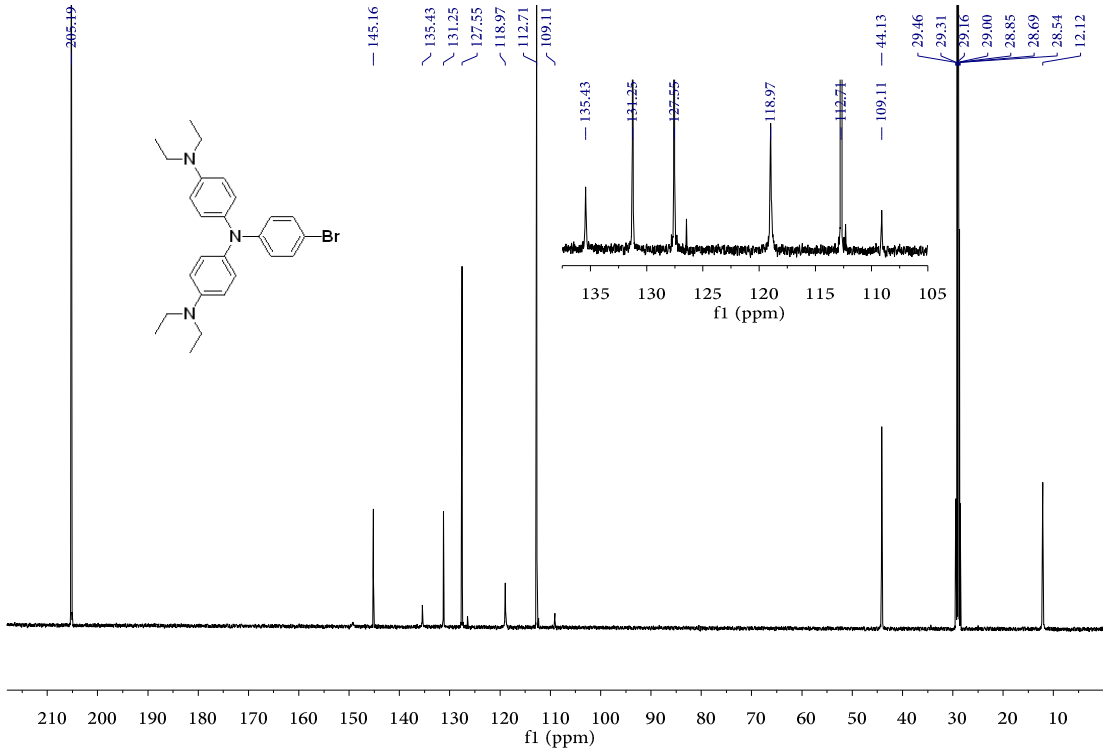

Figure S2. ^{13}C-NMR of Compound 2 in d_6-Acetone, Related to Scheme 1.

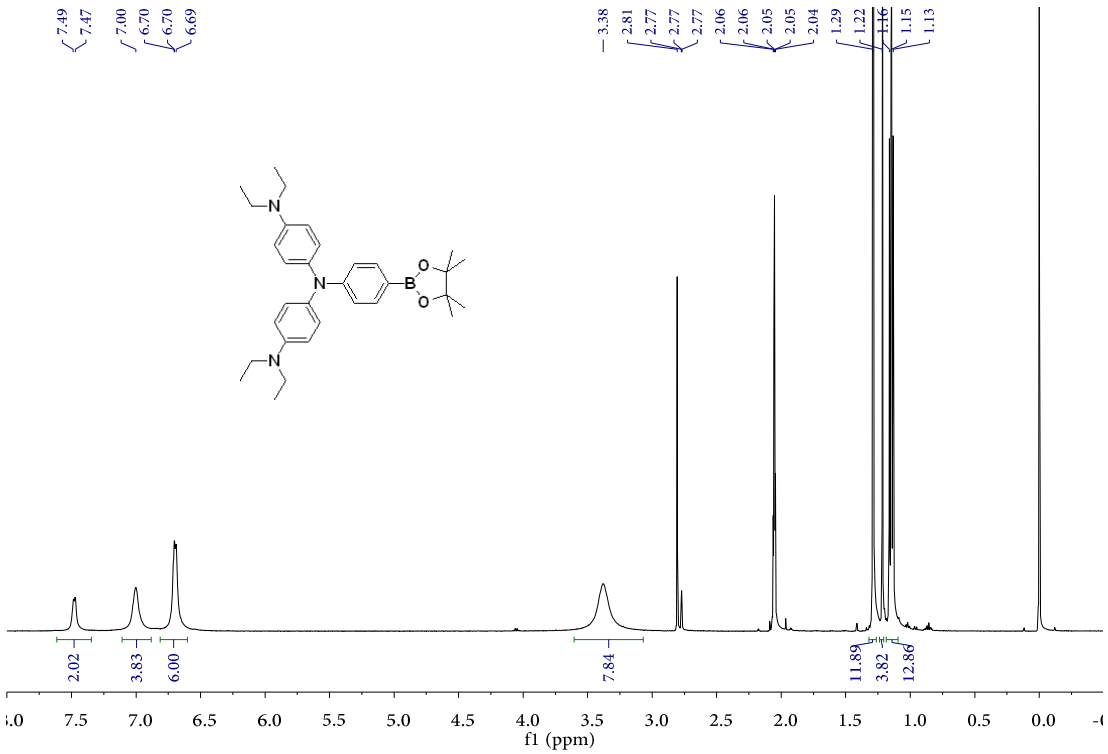

Figure S3. ^{1}H-NMR of Compound 3 in d_6-Acetone, Related to Scheme 1.

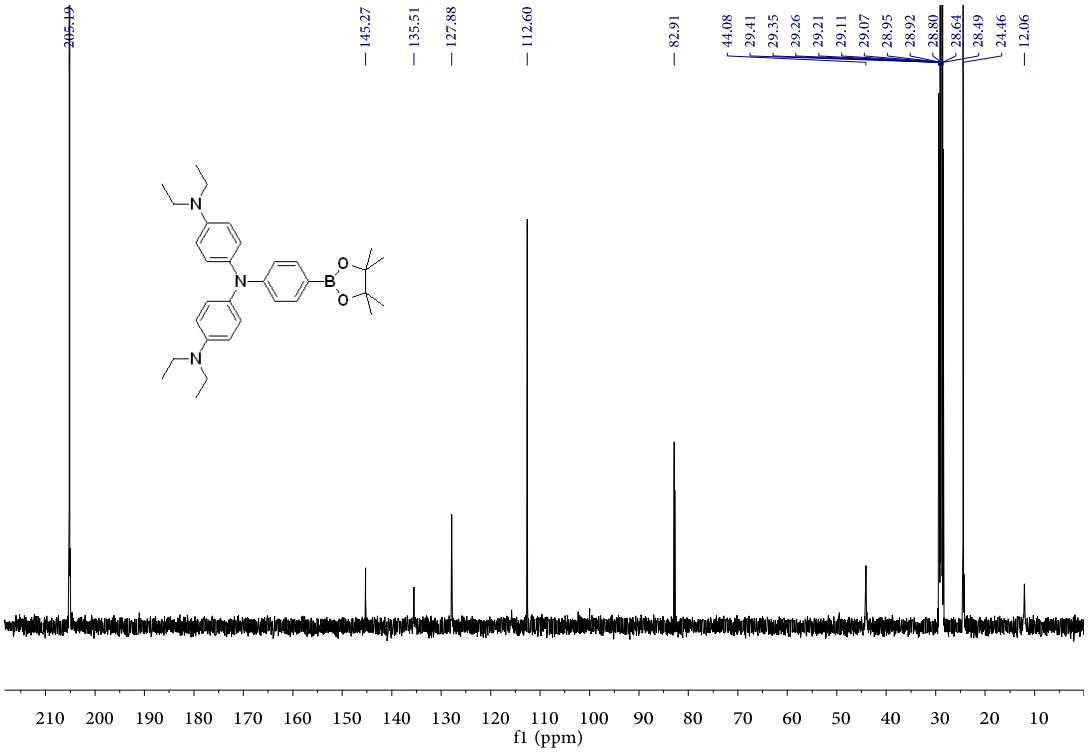

Figure S4. ^{13}C-NMR of Compound 3 in d_6-Acetone, Related to Scheme 1.

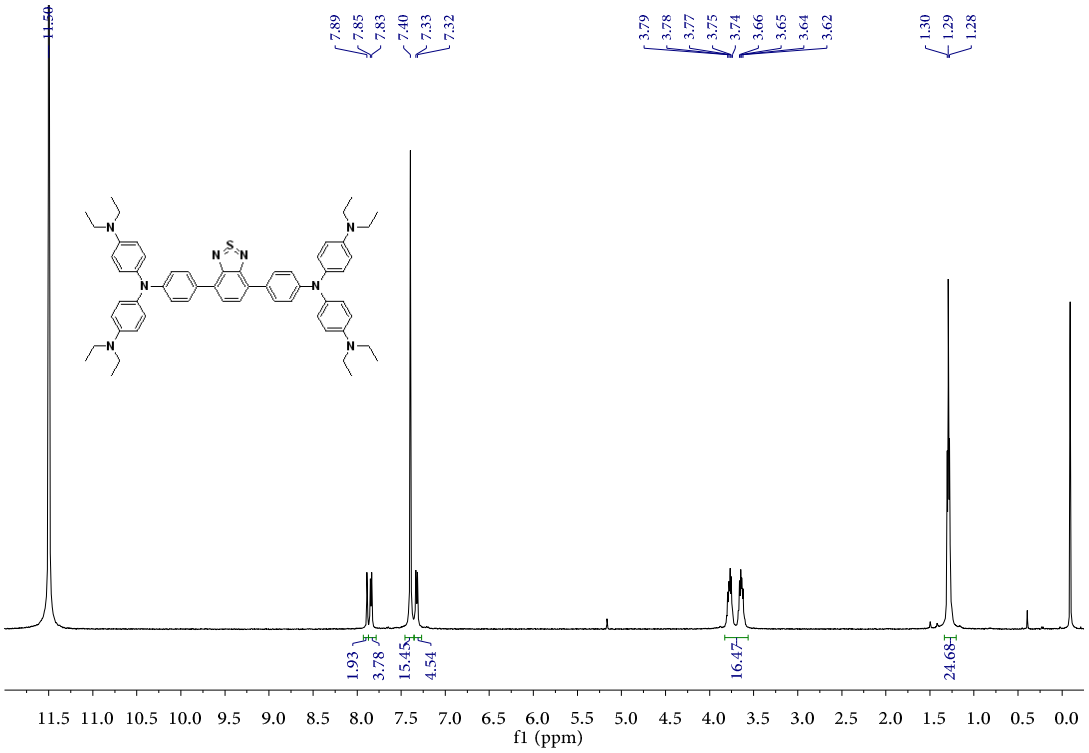

Figure S5. ^{1}H-NMR of TBT in *d*-Trifluoroacetic Acid, Related to Scheme 1.

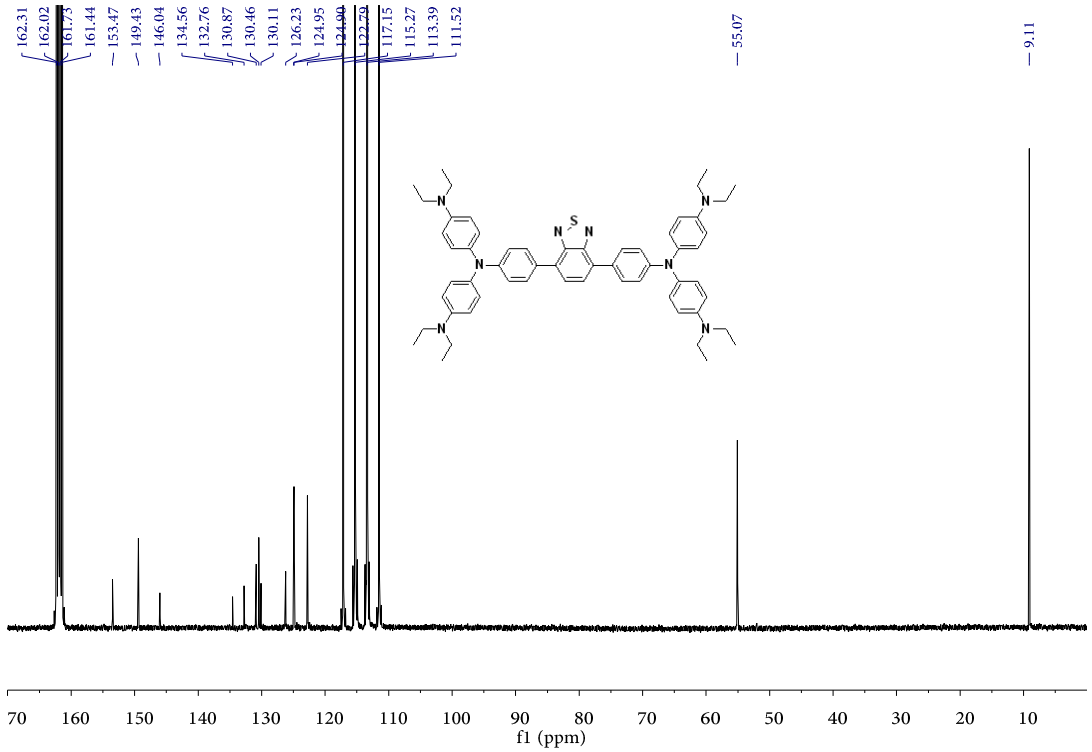

Figure S6. ^{13}C-NMR of TBT in *d*-Trifluoroacetic Acid, Related to Scheme 1.

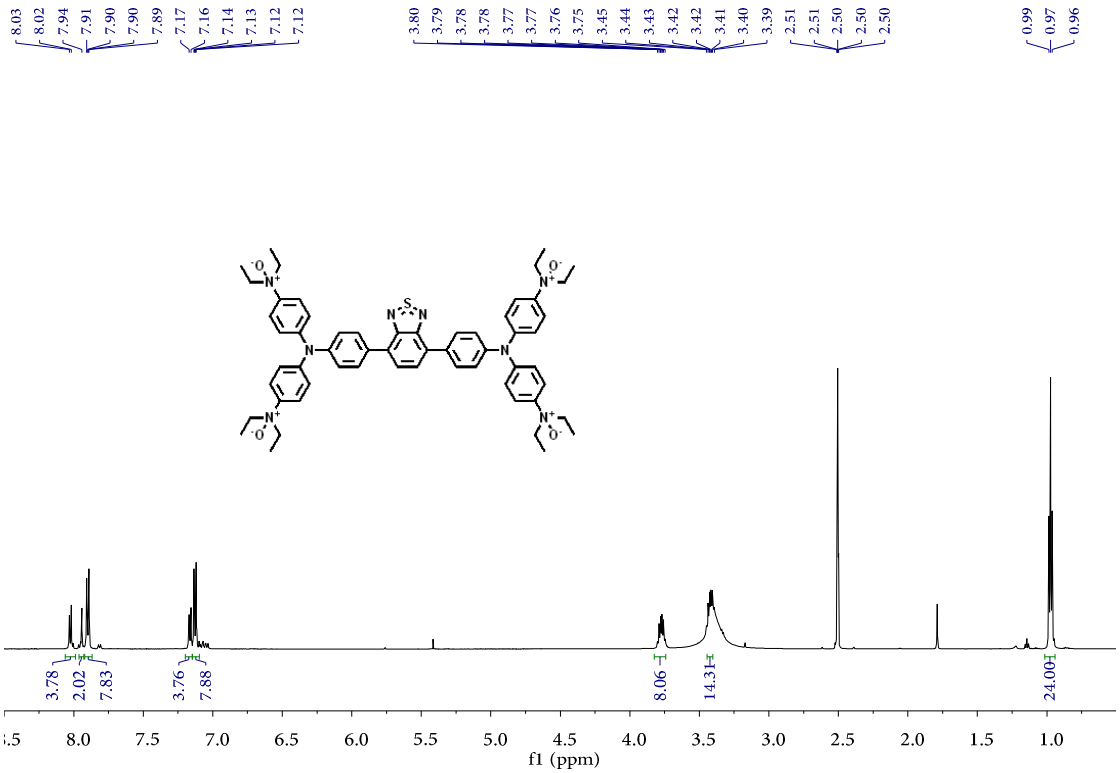

Figure S7. ^{1}H-NMR of TBTO in d_6-Dimethyl Sulfoxide, Related to Scheme 1.

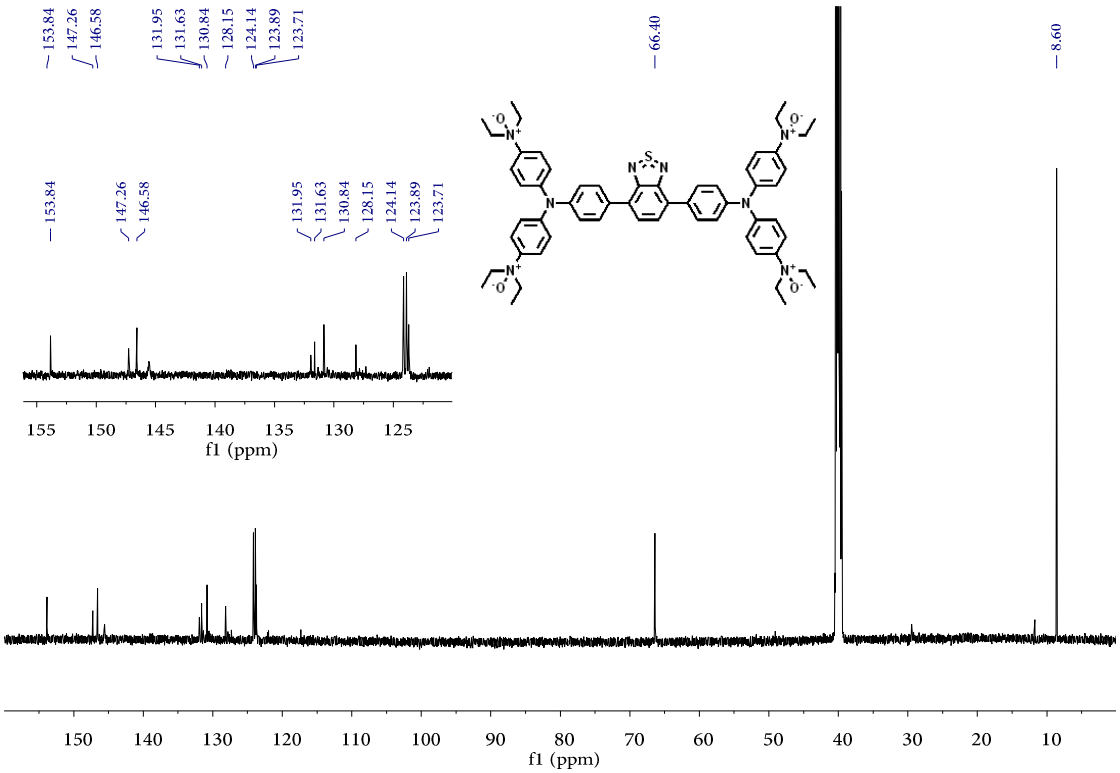

Figure S8. ^{13}C-NMR of TBTO in *d*^{6}-Dimethyl Sulfoxide, Related to Scheme 1.

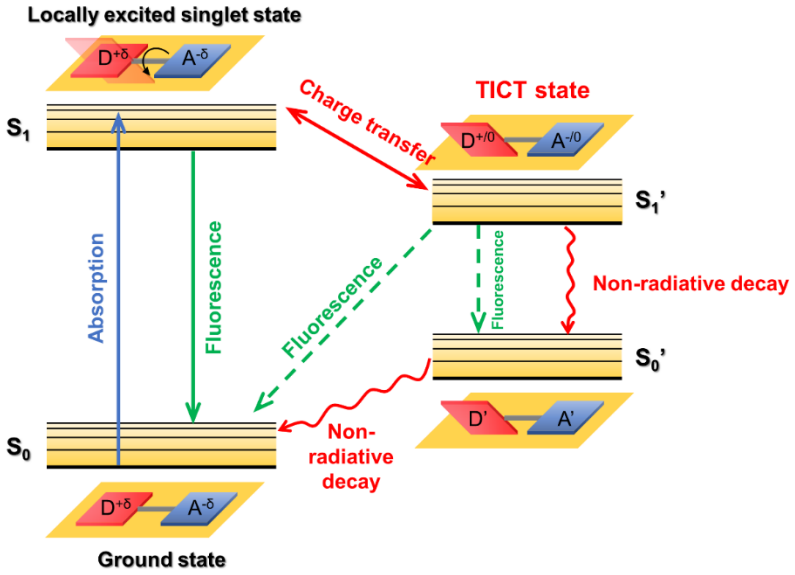

Scheme S2. Jablonski Diagram of TICT Dynamics Referred to Literature Reported (Liu et al., 2019; Sasaki et al., 2016), Related to Scheme 1.

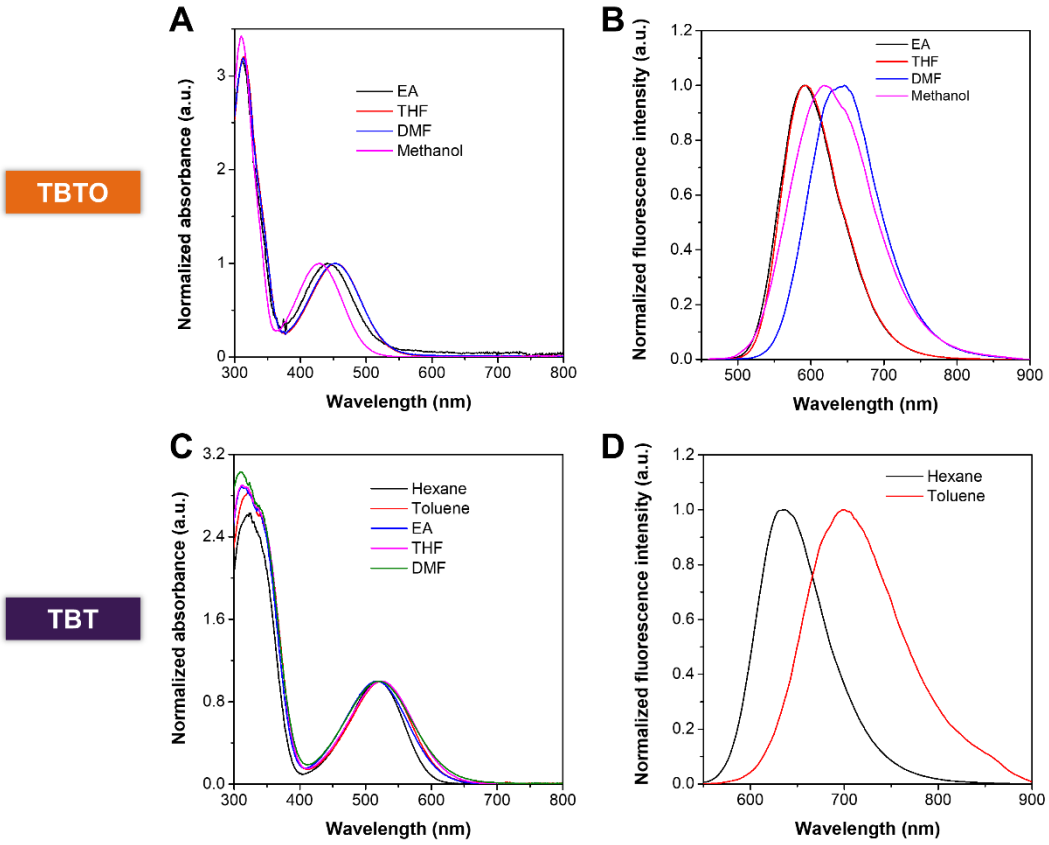

Figure S9. Normalized Absorption and Emission Spectra of TBT and TBTO in Different Solvents, Related to Figure 2. [TBTO], [TBT] = 20 μM.

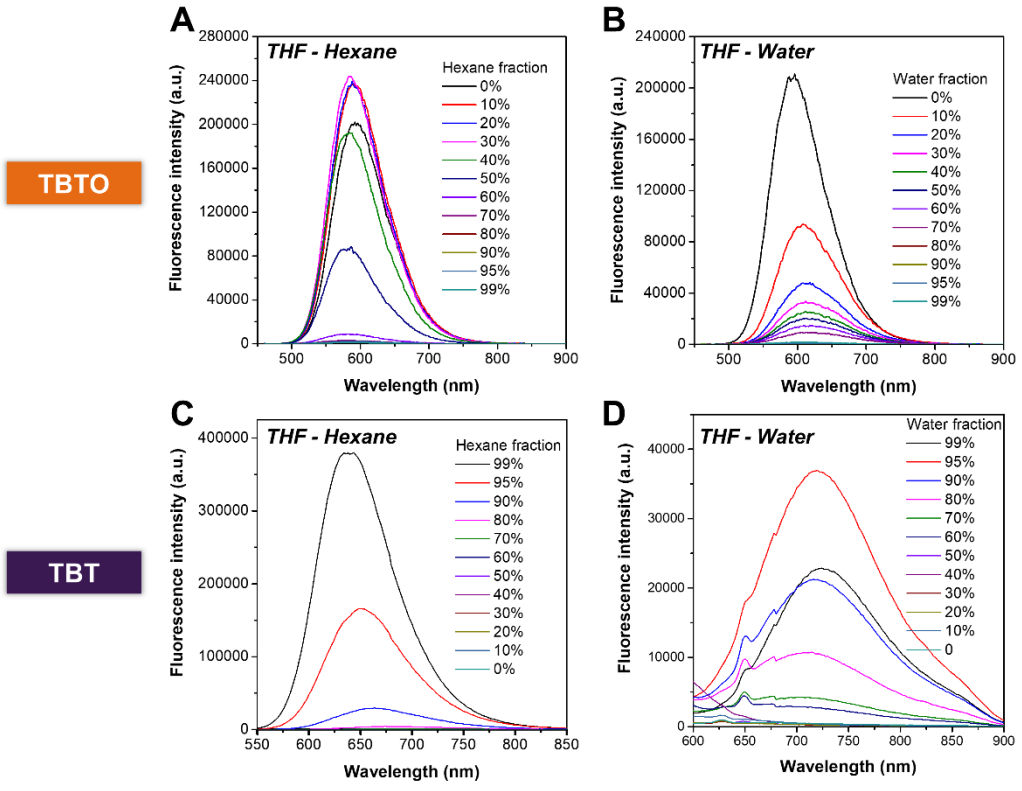

Figure S10. Solvatochromic Effect of TBT and TBTO in the Mixed Solvent System, Related to Figure 2.

Fluorescence emission spectra of (A) TBTO and (C) TBT in THF with different fractions of hexane. Fluorescence emission spectra of (B) TBTO and (D) TBT in THF with different fractions of water. [TBTO], [TBT] = 20 μM.

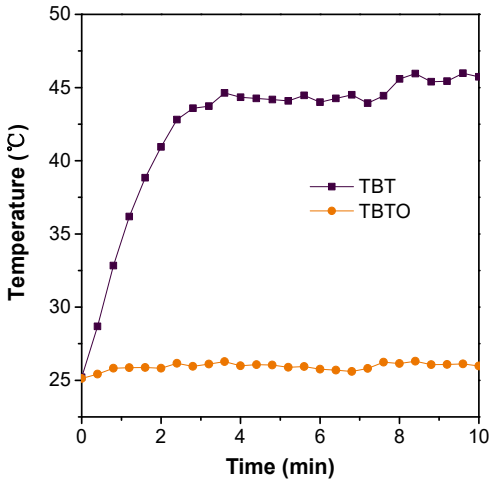

Figure S11. Photothermal Conversion Effect of TBTO and TBT in DMF upon Irradiation with a 660 nm Laser, Related to Scheme 1.

[TBT], [TBTO] = 500 μM. Laser power: 0.5 W/cm^2.

Table S1. Characterizations of TBT NPs and TBTO NPs in Water, Related to Figure 3.

Materials	Size	Zeta potential	$\lambda_{abs,\ max}$	$\lambda_{em,\ max}$	QY
TBTO NPs	50.3 ± 0.7 nm	-22.8 ± 3.8 mV	441 nm	596 nm	3.2%
TBT NPs	103.0 ± 0.6 nm	-41.2 ± 1.2 mV	542 nm	724 nm	0.5%

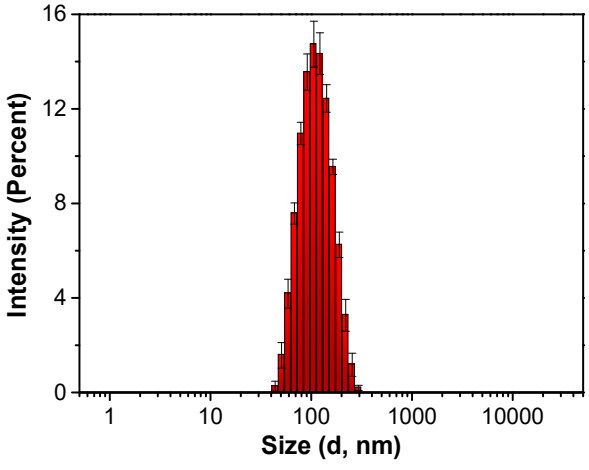

Figure S12. The Size Distribution of TBT NPs in Water, Related to Figure 3.

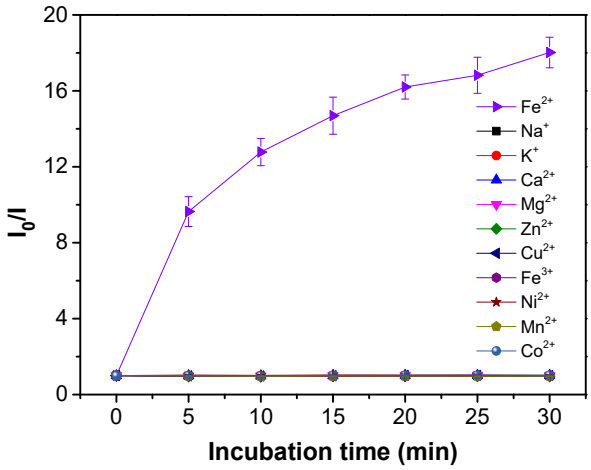

Figure S13. In Vitro Responsiveness of TBTO NPs to Different Metal Ions, Related to Figure 3.

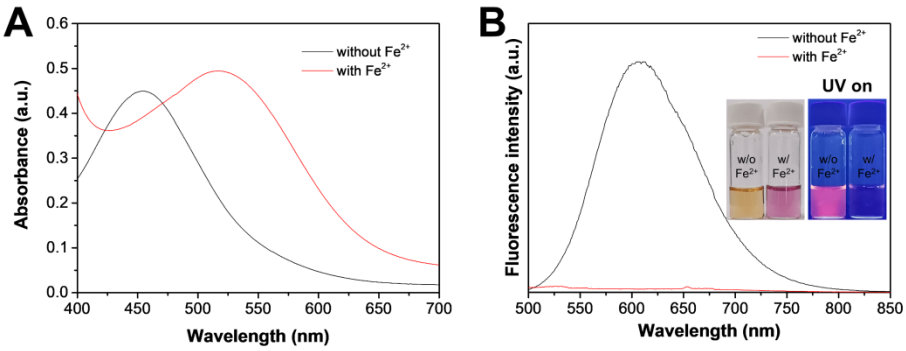

Figure S14. In Vitro Responsiveness of TBTO NPs to Fe(II), Related to Figure 3.
(A) The absorption spectra of TBTO NPs after incubation with or without Fe(II) at 37°C for 2 h. (B) The fluorescence emission spectra of TBTO NPs after incubation with or without Fe(II) at 37°C for 2 h (Insert: the pictures of TBTO NPs solution with or without Fe(II) incubation taken under ambient light or UV lamp).

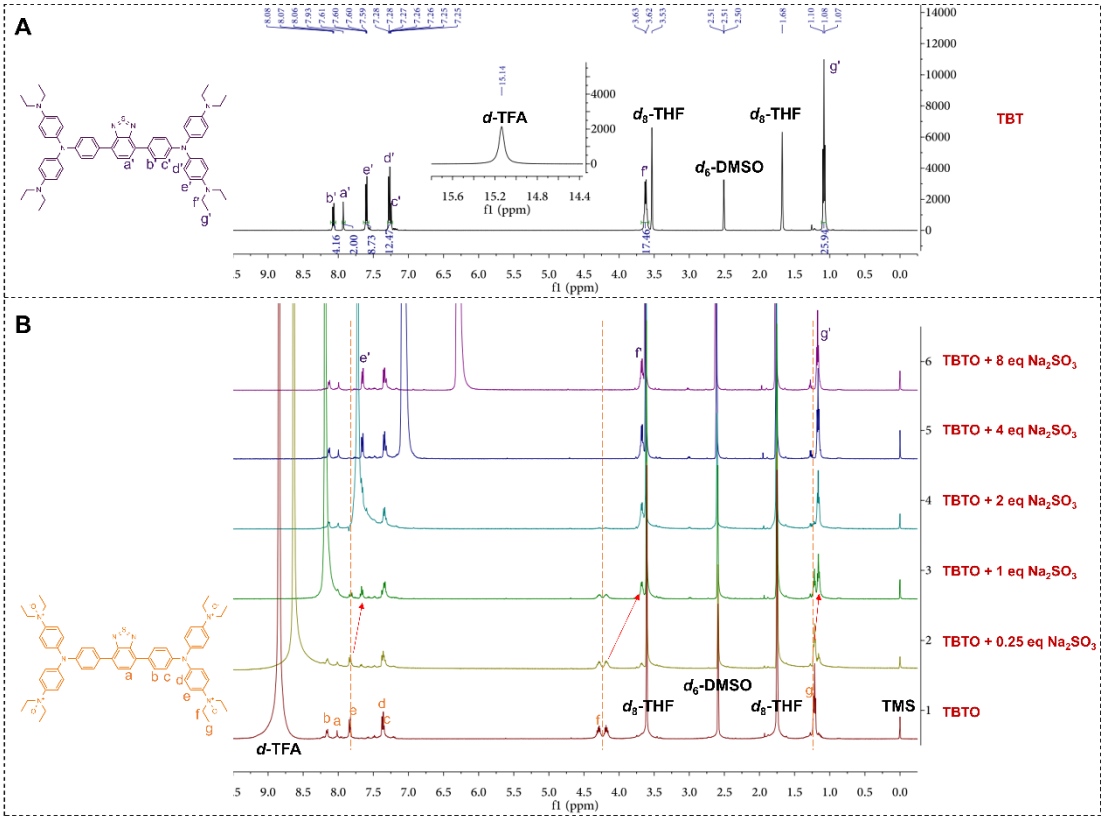

Figure S15. In Vitro Transition of TBTO to TBT Verified by ^{1}H-NMR, Related to Figure 3.

(A) ^{1}H-NMR of TBT in 800 μL of deuterated THF-DMSO-TFA (3.5:3.5:1).

(B) To the solution of TBTO (2 μmol) in 800 μL of deuterated THF-DMSO-TFA (3.5:3.5:1), was added Na_2SO_3 in D_2O (1 M): 2 μL (0.25 eq), 8 μL (1 eq), 16 μL (2 eq), 32 μL (4 eq), and 64 μL (8 eq).

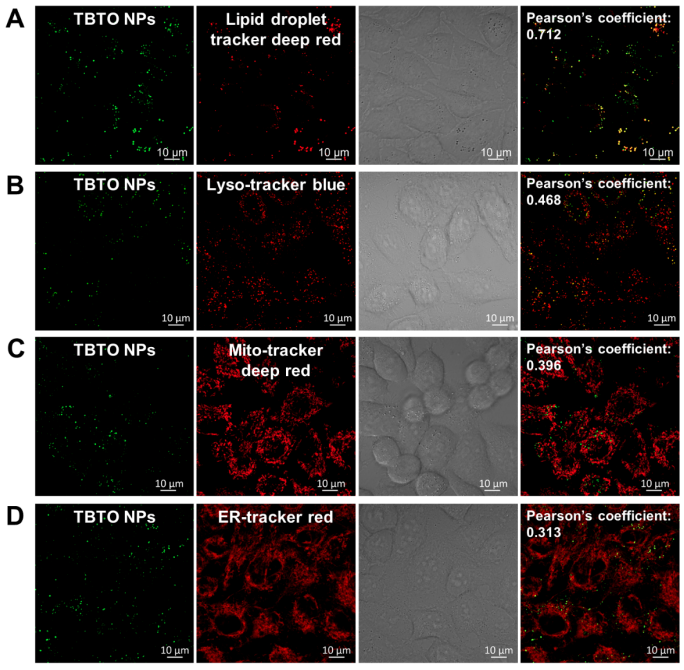

Figure S16. Colocalization Images of TBTO NPs with Different Organelle Trackers,

Related to Figure 3.

CLSM images of HeLa cells incubated with 50 μM TBTO NPs (λ_{ex}: 488 nm; λ_{em}: 610-700 nm) and then 1 μM different organelle trackers: (A) lipid droplet tracker deep red (λ_{ex}: 640 nm; λ_{em}: 645-700 nm), (B) lyso-tracker blue (λ_{ex}: 405 nm; λ_{em}: ＜505 nm), (C) mito-tracker deep red (λ_{ex}: 640 nm; λ_{em}: 645-700 nm), and (D) ER-tracker red (λ_{ex}: 561 nm; λ_{em}: ＜610 nm).

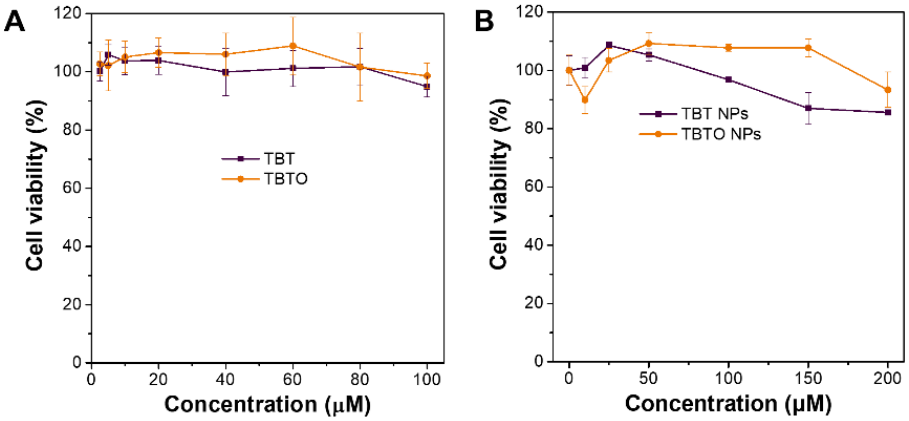

Figure S17. In Vitro Cell Viability of HeLa Cells Against TBT and TBTO in the Form of (A) Bare Molecules or (B) Nanoparticles after Incubation for 24 h, Related to Figure 3.

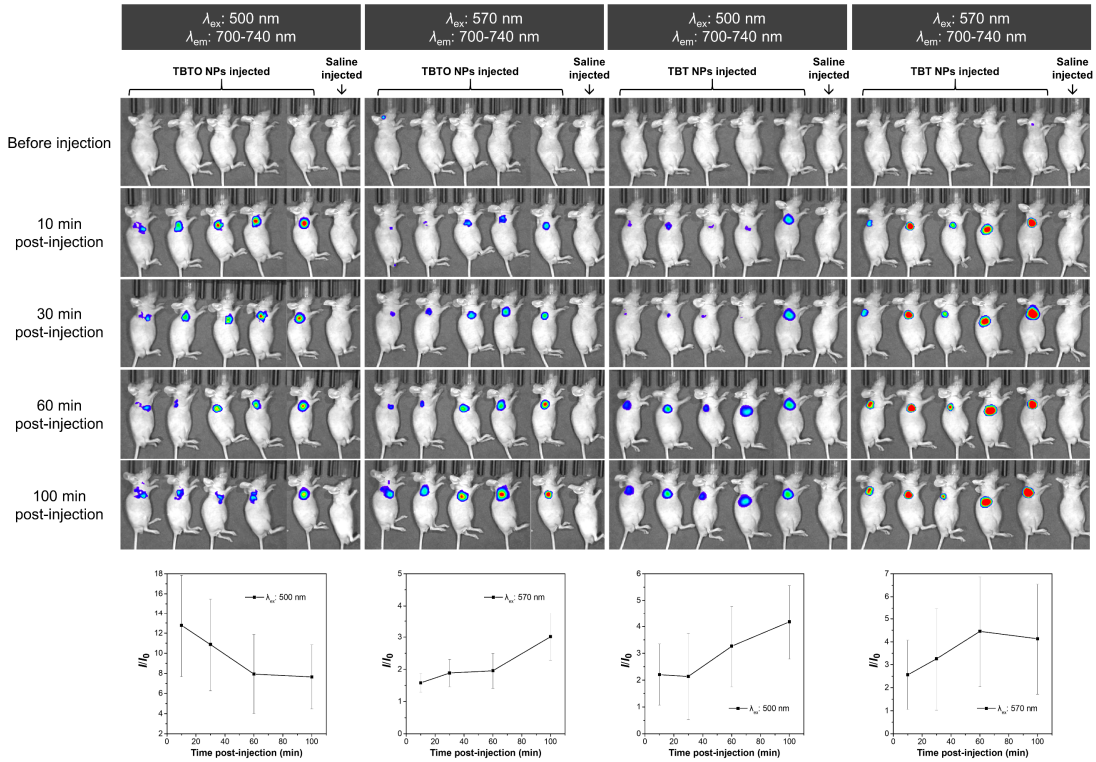

Figure S18. Hypoxia-activated Fluorescence Imaging of TBTO NPs in Vivo, Related to Figure 4.

Time-lapse NIR fluorescence imaging of mice before and after intratumoral injection with TBTO NPs or TBT NPs (50 μL, 1 mg/mL) and semiquantitative analysis of fluorescence intensities in the tumor site of the mice as a function of time. The fluorescence signals were

collected upon excitation with 500 nm and 570 nm, respectively.

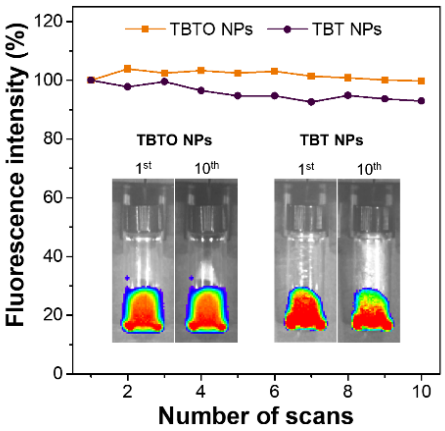

Figure S19. Photostability of TBTO NPs and TBT NPs, Related to Figure 4.

The fluorescence intensities of TBTO NPs (λ_{ex}: 500 nm) and TBT NPs (λ_{ex}: 570 nm) upon illumination with the laser in the small animal imaging system for 10 times.

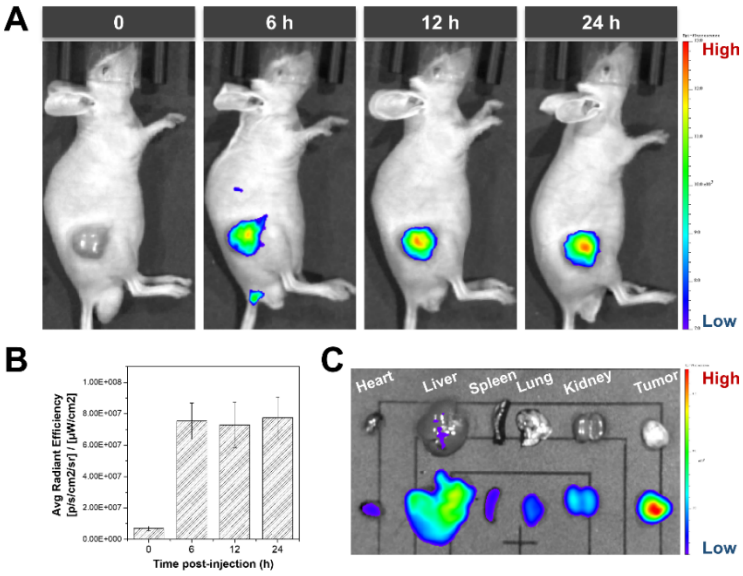

Figure S20. Fluorescence Imaging of TBTO NPs in Tumor-bearing Mice via Tail Intravenous Injection, Related to Figure 4.

(A) Time-lapse NIR fluorescence imaging of mice before (time point: 0 min) and after tail intravenous injection with TBTO NPs.

(B) Semiquantitative analysis of fluorescence intensities in the tumor site of the mouse injected with TBTO NPs.

(C) Ex vivo NIR fluorescence images of major organs and tumors after injection with PBS (the upper row) and TBTO NPs (the lower row) for 24 h.

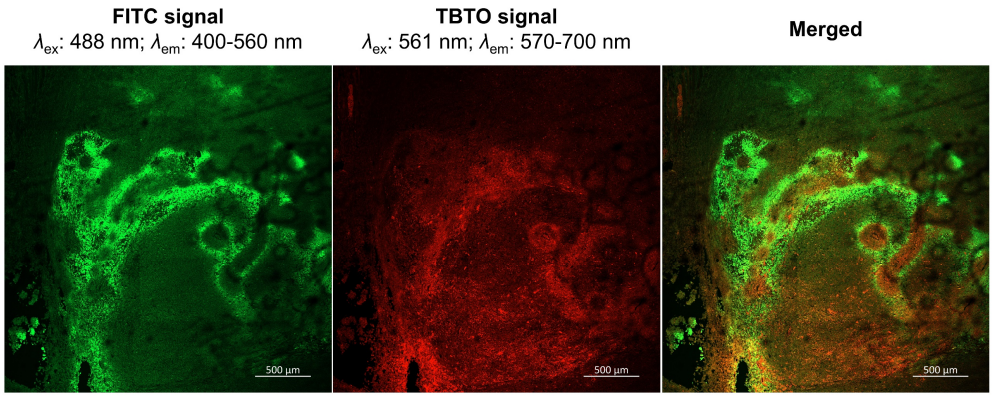

Figure S21. Ex Vivo Colocalization of TBTO Signal in Tumor Site with a Commercial Hypoxia Imaging Kit Using Immunofluorescence Staining Method, Related to Figure 4.

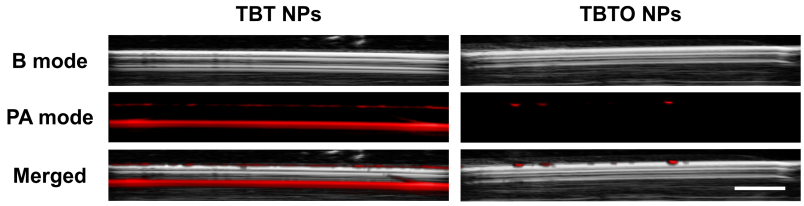

Figure S22. In Vitro PA Imaging of TBTO NPs and TBT NPs in FEP Tubes, Related to Figure 5. Scale bar represents 2 mm.

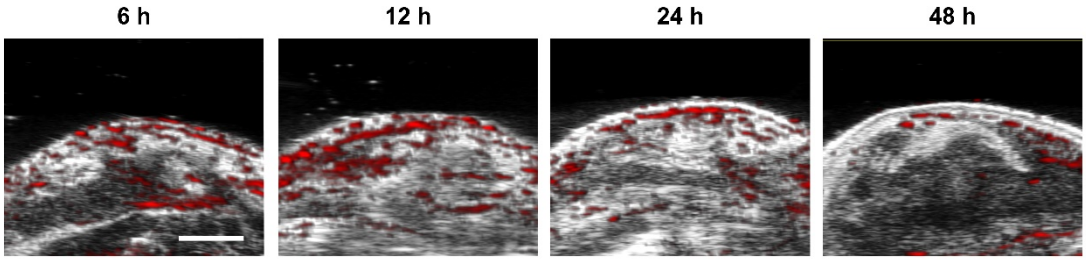

Figure S23. In Vivo PA Imaging with TBT NPs, Related to Figure 5.
In vivo PA images of the tumor site in the mice after tail intravenous injection with TBT NPs (200 μL, 1 mg/mL). Scale bar represents 2 mm.

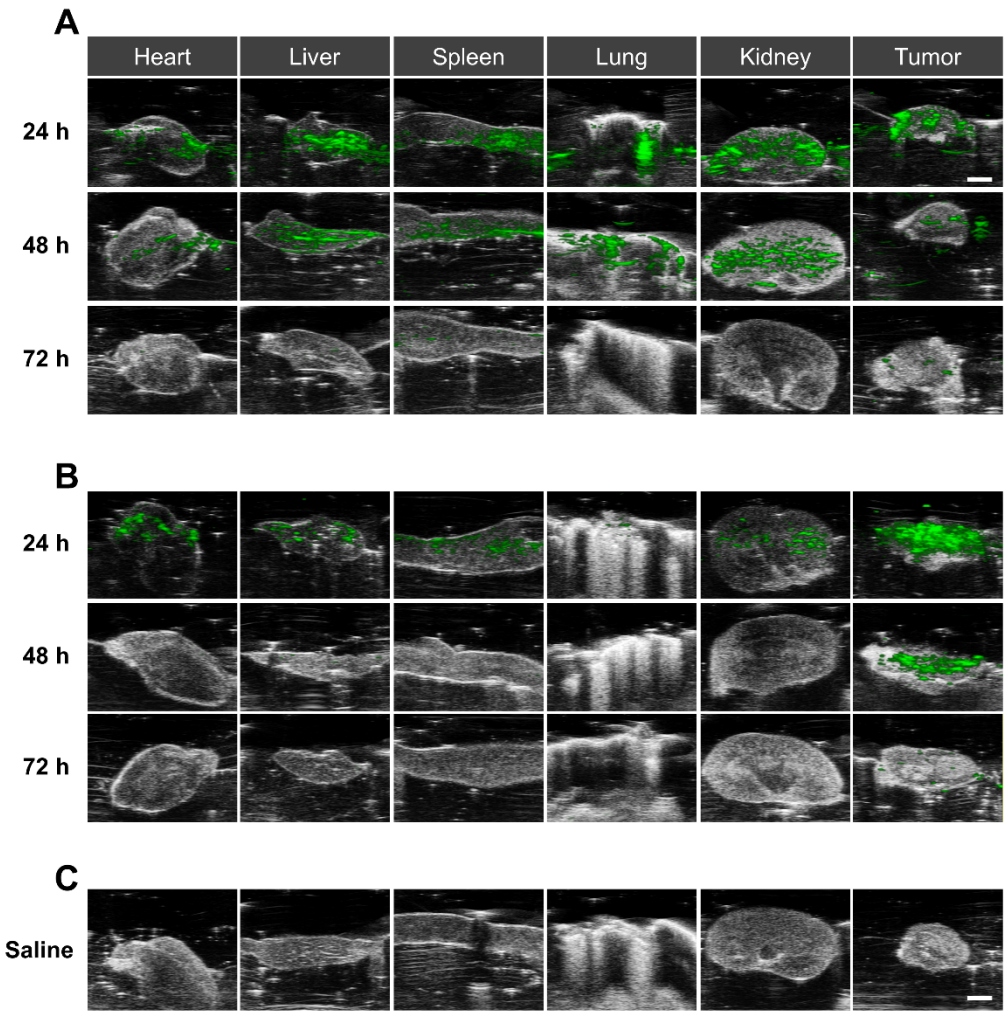

Figure S24. Bioelimination of TBTO NPs from Major Organs and Tumors, Related to Figure 5.

(A) PA images of major organs and tumors at different time points after tail intravenous injection of TBTO NPs.

(B) PA images of major organs and tumors at different time points after intratumoral injection of TBTO NPs.

(C) PA images of major organs and tumors at different time points after tail intravenous injection of saline. Scale bar: 2 mm.

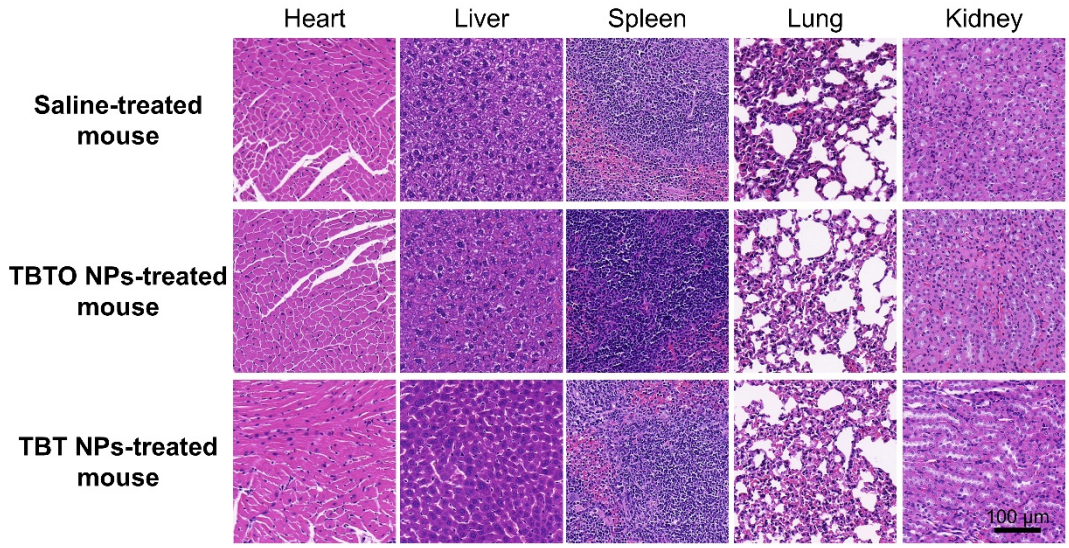

Figure S25. H&E Staining Images of the Major Organs after Intravenous Injection of (A) TBTO NPs and (B) TBT NPs via Tail Vein for 72 h, Related to Figure 5.

Transparent Methods

Materials and instruments:

DSPE-mPEG2000 with a methoxy terminal group (1,2-distearoyl-sn-glycero-3-phosphoethanolamine-N-[methoxy(polyethylene glycol)-2000], CAS: 147867-65-0) was purchased from Xi'an Ruixi Biological Technology Co., Ltd. ER-Tracker Red (Cat. No. C1041) for endoplasmic reticulum staining was purchased from Beyotime Biotechnology (Shanghai, China). LysoBlue (Cat. No. KGMP006-1) for lysosome staining was purchased from Jiangsu KeyGEN BioTECH Co., Ltd (Nanjing, China). HCS LipidTOX Deep Red Neutral (Cat. No. H34477) for lipid droplet staining and MitoTracker Deep Red FM (Cat. No. M22426) for mitochondria staining were purchased from Thermo Fisher Scientific Inc (USA). Dulbecco's Modified Eagle Medium (DMEM) with high glucose, phosphate buffer saline, fetal bovine serum (FBS), and penicillin/streptomycin were purchased from Thermo Fisher Scientific Inc. Hypoxyprobe Green Kit-1 (Cat. No. HP6-100kit), a commercial hypoxia imaging kit containing pimonidazole HCl (Hypoxyprobe-1) and FITC-conjugated anti-pimonidazole mouse IgG_1 monoclonal antibody (FITC-MAb1), was purchased from Hypoxyprobe Inc (USA). All the chemicals and reagents were purchased from Shanghai Aladdin Biochemical Technology Co., Ltd. or J&K Scientific Ltd. and they were used as purchased without further purification. AnaeroPack™ anaerobic gas generator, 2.5 L rectangular sealed container, and anaero-indicators were purchased from Mitsubishi Chemical Corporation.

All the NMR spectra were recorded on a Bruker AVANCE III 500 MHz and 600 MHz (Bruker, Germany). High-resolution mass spectra (HR-MS) were recorded on an AB SCIEX Triple TOF 6600 (AB SCIEX, USA). UV-vis absorption spectra were recorded on a PerkinElmer Lambda 950 (Perkin-Elmer, USA). Fluorescence emission spectra were recorded on an FS 5 fluorescence spectrometer (Edinburgh Instruments, UK). The absolute photoluminescence quantum yield was determined by Hamamatsu Quantaurus-QY (Hamamatsu Photonics, Japan). The size distribution of nanoparticles was tested with a dynamic light scattering (DLS) method using a Malvern Zetasizer Nano series (Malvern Instruments, Inc., UK). Particle size and morphology were observed on a Hitachi HT7700 transmission electron microscope. CLSM images were taken on an LSM880 (Carl Zeiss AG, Germany). Photothermal conversion performance was monitored by an E6 IR-camera (FLIR, USA). In vivo fluorescence imaging was performed using an IVIS Spectrum live-animal imaging system (Perkin-Elmer, USA). PA imaging was performed using a Vevo LAZR-X (Fuji Film Visual Sonics, USA).

The synthesis of compound 2:

Compound 1 was synthesized according to known procedures and the ^{1}H-NMR datum matches that reported in the literature. (Tancini et al., 2012) To the solution of compound 1 (1.4 g, 5 mmol) and 4-bromoaniline (344 mg, 2 mmol) in 10 mL of toluene, was added KOH (1.8 g, 32 mmol), 1, 10-phenanthroline (36 mg, 0.2 mmol) and CuI (38 mg, 0.2 mmol). The resulting mixture was cooled to 0°C, degassed, and then flushed with N_2 for three cycles. The reaction was heated at 125°C under an N_2 atmosphere for 24 hours and then cooled down to room temperature. The reaction mixture was diluted in dichloromethane, washed with 1 M HCl

solution and brine, dried over anhydrous sodium sulfate, and concentrated in a vacuum. The crude mixture was purified by silica gel (200-300 mesh) column chromatography (petroleum ether: ethyl acetate = 25:1) to afford the pure product as an off-white solid (720 mg, 77% yield).
^{1}H NMR (500 MHz, Acetone-d_6) δ 7.27 – 7.11 (m, 2H), 6.97 (d, *J* = 8.6 Hz, 4H), 6.71 – 6.54 (m, 6H), 3.36 (p, *J* = 7.5 Hz, 8H), 1.12 (t, *J* = 7.1 Hz, 12H).
^{13}C NMR (126 MHz, Acetone-d_6) δ 145.16, 135.43, 131.25, 127.55, 118.97, 112.71, 109.11, 44.13, 12.12.
HR-MS (TOF) m/z: $[M+H]^+$ Calc'd for $C_{26}H_{33}N_3Br^+$ 466.1853 and 468.1832; Found 466.1850 and 468.1828.

The synthesis of compound 3:
To the solution of compound 2 (757 mg, 1.6 mmol) and bis(pinacolato)diboron (620 mg, 2.44 mmol) in 15 mL of 1.4-dioxane was added potassium acetate (798 mg, 8.14 mmol) and $Pd(dppf)Cl_2$ (50 mg). The resulting mixture was cooled to 0°C, degassed, and then flushed with N_2 for three cycles. The reaction was heated at 80°C under an N_2 atmosphere for 12 hours and then cooled down to room temperature. The reaction mixture was diluted in ethyl acetate, washed with brine three times, dried over anhydrous sodium sulfate, and concentrated in a vacuum. The crude mixture was purified by silica gel (200-300 mesh) column chromatography (petroleum ether: ethyl acetate = 10:1) to afford the pure product as a pale yellow solid (712 mg, 85% yield).
^{1}H NMR (500 MHz, Acetone-d_6) δ 7.48 (d, J = 8.1 Hz, 2H), 7.00 (s, 4H), 6.81 – 6.60 (m, 6H), 3.38 (m, 8H), 1.29 (s, 12H), 1.15 (t, J = 7.0 Hz, 12H).
^{13}C NMR (126 MHz, Acetone-d_6) δ 145.27, 135.51, 127.88, 112.60, 82.91, 44.08, 24.46, 12.06.
HR-MS (TOF) m/z: $[M+H]^+$ Calc'd for $C_{32}H_{45}BN_3O_2^+$ 514.3599; Found 514.3602.

The synthesis of TBT:
To the solution of compound 3 (712 mg, 1.4 mmol) and 4,7-dibromo-2,1,3-benzothiadiazole (136 mg, 0.46 mmol) in 10 mL of 1,4-dioxane and 2 mL of water, was added potassium carbonate (510 mg, 3.7 mmol) and 60 mg $Pd(PPh_3)_4$. The resulting mixture was cooled to 0°C, degassed, and then flushed with N_2 for three cycles. The reaction was heated at 100°C under an N_2 atmosphere for 24 hours and then quenched with water. The aqueous layer was extracted with dichloromethane three times, dried over sodium sulfate, and concentrated in a vacuum. The crude mixture was purified by silica gel (200-300 mesh) column chromatography (petroleum ether: ethyl acetate = 4:1) to afford the pure product as a magenta solid (403 mg, 89% yield).
^{1}H NMR (500 MHz, Trifluoroacetic acid-*d*) δ 7.89 (s, 2H), 7.84 (d, *J* = 8.1 Hz, 4H), 7.40 (s, 16H), 7.32 (d, *J* = 8.2 Hz, 4H), 3.71 (ddd, *J* = 66.6, 13.2, 7.2 Hz, 16H), 1.29 (t, *J* = 7.1 Hz, 24H).
^{13}C NMR (151 MHz, Trifluoroacetic acid-*d*) δ 153.47, 149.43, 146.04, 134.56, 132.76, 130.87, 130.46, 130.11, 126.23, 124.90, 122.79, 55.07, 9.11.
HR-MS (TOF) m/z: $[M+H]^+$ Calc'd for $C_{58}H_{67}N_8S^+$ 907.5204; Found 907.5226. $[M+2H]^{2+}$ Calc'd for $C_{58}H_{68}N_8S^{2+}$ 454.2638; Found 454.2653.

The synthesis of TBTO:

To the solution of TBT (90.7 mg, 0.1 mmol) in 5 mL of dichloromethane, was added $NaHCO_3$ (37 mg, 0.44 mol). The solution was cooled to 0°C and 3-chloroperbenzoic acid (*m*-CPBA, 76 mg, 0.44 mmol) was added with vigorous stirring. The color of the mixture turned from magenta to orange-yellow within 10 min. The reaction was warmed up to room temperature and furthered stirred for 2 hours and then purified by aluminum oxide (300-400 mesh) column chromatography (dichloromethane: methanol = 20:1) to afford a yellow color powder (75 mg, 77%).

^{1}H NMR (600 MHz, DMSO-d_6) δ 8.02 (d, *J* = 8.7 Hz, 4H), 7.94 (s, 2H), 7.92 – 7.87 (m, 8H), 7.16 (d, *J* = 8.7 Hz, 4H), 7.15 – 7.10 (m, 8H), 3.77 (dq, *J* = 11.6, 6.9 Hz, 8H), 3.45 – 3.40 (m, 8H), 0.97 (t, *J* = 7.0 Hz, 24H).

^{13}C NMR (151 MHz, DMSO-d_6) δ 153.84, 147.26, 146.58, 131.95, 131.63, 130.84, 128.15, 124.14, 123.89, 123.71, 66.40, 8.60.

HR-MS (TOF) m/z: $[M+H]^+$ Calc'd for $C_{58}H_{67}N_8O_4S^+$ 971.5000; Found 971.5000.

The preparation of TBTO NPs:

1 mg of TBTO was dissolved in 1 mL of THF and then added to 9 mL of ultrapure water containing 5 mg of DSPE-mPEG2000 in an ice bath, followed by sonication with a probe sonicator at an output power of 45% for 2 min (on/off cycle: 3 s/2 s). The resulting mixture was concentrated by ultrafiltration, washed with ultrapure water to remove THF, and then lyophilized and kept at 4°C for later use. For quantification of TBTO in nanoparticles, the lyophilized TBTO NPs were dissolved in DMSO and the loading content of TBTO was calculated using a pre-established calibration absorption curve of TBTO. The particle size, zeta potential, and morphology of TBTO NPs were examined by DLS and TEM.

Fe(II) sensing of TBTO NPs in vitro:

To 100 μL of TBTO NPs solution (50 μM) in PBS buffer (0.1 M, pH 7.4) in a 96-well plate was added 2 μL of metal ions solution in water (25 mM). The fluorescence intensity of TBTO at 600 nm (Ex: 450 nm) was monitored by a microplate reader (BioTek Synergy H1) before or after the treatment of metal ions for different time intervals. The working temperature of the microplate reader was set to 37°C.

The photothermal performance measurement of TBT and TBTO:

TBT and TBTO were dissolved in 200 μL of DMF-H_2O (1:1) at the concentration of 500 μM and then irradiated with a 660 nm laser at a power density of 0.5 W/cm^2 for 10 min. The temperature was recorded every 20 seconds.

Cell culture:

Human cervical cancer HeLa cell line was purchased from The Cell Bank of Type Culture Collection of Chinese Academy of Sciences and cultured in Dulbecco's Modified Eagle Medium (DMEM) with high glucose containing 10% Fetal Bovine Serum (FBS) and 1% antibiotics (penicillin-streptomycin) at 37°C in a humidified environment. Cells were culture in 5%CO_2 and 20% O_2 for normoxic conditions. Hypoxic cells were culture in 5% CO_2 and 0% O_2 in a sealed container (Mitsubishi, D-110) with an anaerobic gas generator (Mitsubishi, D-07), and the O_2 level was monitored by an anaero-indicator (Mitsubishi, D-66).

Cell cytotoxicity tests of TBTO and TBT:

HeLa cells were sub-culture into a 96 well plate with a density of 5×10^3 cells per well. After incubation at 37°C overnight for cell adherence, cells were treated with different concentrations of TBTO or TBT and then further cultured for 24 h. After that, cells were treated with MTT solution at a concentration of 0.5 mg/mL and then incubated for 4 h. MTT solution was discarded and 100 μL of DMSO was added per well, followed by a rigid shaking for 2 min to dissolve all the precipitates. The absorbance at 450 nm was measured by a microplate reader and the relative cell viability was calculated by the following equation: cell viability (%) = $(OD_{sample} - OD_{background}) / (OD_{control} - OD_{background}) \times 100\%$.

Hypoxia responsiveness of TBTO NPs at a cellular level:

HeLa cells were sub-cultured into a 48 well plate with a density of 2.5×10^4 cells per well. After incubation at 37°C for 36 h to an 80% confluency, cells were transferred to either a standard atmosphere containing 20% oxygen (normoxic condition) or a sealed container with an anaerobic gas generator to keep the oxygen level lower than 0.1% (hypoxic condition). After pre-incubation for 12 h in the above conditions, cells were treated with different concentrations of TBTO NPs in an FBS-free medium and then a further incubation for 3 h in normoxic or hypoxic conditions. After that, the fluorescence intensities at 600 nm with an excitation of 450 nm of the cell culture supernatants were measured in a microplate reader. The FBS-free medium without TBTO NPs treatment was used as blank to deduct the background emission.

Tumor model establishment:

The male BALB/c nude mice (4~5 weeks) were obtained from Beijing Vital River Laboratory Animal Technology, and all the performances of in vivo experiments followed the protocols approved by the Administrative Committee on Animal Research in Shenzhen Graduate School, Peking University. A suspension of 5×10^6 HeLa cells in PBS (150 μL) was subcutaneously injected into each mouse to construct the tumor model. After about 7 days, mice with tumor volume at about 100 mm^3 were used for in vivo experiments.

In vivo NIR fluorescence imaging:

The hydrolyzed nanoparticles were dissolved in saline right before use.

Intratumoral injection: Two tumor-bearing mice were anesthetized with isoflurane and administered TBTO NPs and TBT NPs (50 μL, 1 mg/mL) via intratumoral injection, respectively. Immediately after that, these two mice were transferred to the small animal imaging system and imaged with excitation filters of 500 nm and 570 nm and corresponding emission filters of 720 and 740 nm. Data were processed using Living Image software (Version 4.5). ROIs with the equal area were drawn in the tumor site of each image, and average radiant efficiency in each ROIs was measured.

Tail intravenous injection: Two tumor-bearing mice were administered TBTO NPs via tail intravenous injection (200 μL, 1 mg/mL). At different time points post-injection, mice were anesthetized with isoflurane and imaged with a small animal imaging system with an excitation filter of 570 nm and corresponding emission filters of 720 and 740 nm. After 24 h, mice were sacrificed; the organs and tumors were imaged using the same filter as above. Data were

processed using Living Image software (Version 4.5). ROIs with the equal area were drawn in the tumor site of each image, and average radiant efficiency in each ROIs was measured.

Ex vivo colocalization with commercial hypoxia imaging kit

Three tumor-bearing mice were administered TBTO NPs via tail intravenous injection (200 μL, 1 mg/mL in saline). After normal feeding for 24 h, mice were then administered pimonidazole HCl (Hypoxyprobe-1, 100 μL, 2.8 mg/mL in saline) via tail intravenous injection and then sacrificed after 2 h. Tumors were harvested and then immunofluorescence staining in formalin-fixed and paraffin-embedded tissue sections was performed using FITC-conjugated anti-pimonidazole mouse IgG_1 monoclonal antibody (FITC-MAb1). Fluorescence images were acquired using CLSM with a tile mode to stitch 25 images to a large field of view.

In vitro PA imaging in tissue-mimicking phantoms:

Tissue phantoms were prepared referring to a literature reported method (Knox et al., 2018). In brief, agarose (4 g) was suspended in a solution of 2% milk (2 mL) and distilled water (78 mL) and then heated in a microwave oven for 1 min. The obtained viscous gel was transferred to a 50 mL centrifuge tube with a FEP tube (2 mm inner diameter, 10 cm long, sealed with cotton at the bottom) inside. After cooling for 3 h, the solidified phantom was removed from the centrifuge tube and cut with a knife so that the phantom was around 2 cm thick with the FEP tube in the middle. TBTO NPs or TBT NPs aqueous solution was filled in the FEP tube using a syringe with a long needle and then imaged with Vevo LAZR-X.

In vivo PA imaging:

The hydrolyzed nanoparticles were dissolved in saline right before use. Mice were administered TBTO NPs via tail intravenous injection (200 μL, 1 mg/mL) or intratumoral injection (200 μL, 1 mg/mL). After different time intervals post-injection, mice were then anesthetized with isoflurane, and images were acquired using the Step and Shoot mode with 100 angles and 15 pulses per angle. Mice were then sacrificed at different time points post-injection: 1 day, 2 days, and 3 days to check the bioelimination in different organs and tumors. Data were analyzed using Vevo LAB 3.2.0 software. Thick slab processing was used to visualize accumulated signals over 12 mm.

SUPPLEMENTAL REFERENCES

Tancini, F., Wu, Y.-L., Schweizer, W.B., Gisselbrecht, J.-P., Boudon, C., Jarowski, P.D., Beels, M.T., Biaggio, I., and Diederich, F. (2012). 1,1-Dicyano-4-[4-(diethylamino)phenyl]buta-1,3-dienes: structure–property relationships. Eur. J. Org. Chem. *2012*, 2756-2765.